Accepted Manuscript

N.D. Charisiou, L. Tzounis, V. Sebastian, S.J. Hinder, M.A. Baker, K. Polychronopoulou, M.A. Goula

Investigating the correlation between deactivation and the carbon deposited on the surface of Ni/Al₂O₃ and Ni/La₂O₃-Al₂O₃ catalysts during the biogas reforming reaction

N.D. Charisiou[1], L. Tzounis[2], V. Sebastian[3,4], S.J. Hinder[5], M.A. Baker[5], K. Polychronopoulou[6], M.A. Goula[1,*]

[1]*Laboratory of Alternative Fuels and Environmental Catalysis (LAFEC), Department of Environmental and Pollution Control Engineering, Western Macedonia University of Applied Sciences, GR-50100, Greece*

[2]*Composite and Smart Materials Laboratory (CSML), Department of Materials Science & Engineering, University of Ioannina, GR-45110, Ioannina, Greece*

[3]*Chemical and Environmental Engineering Department & Nanoscience Institute of Aragon (INA), University of Zaragoza, Zaragoza, SP-50018, Spain*

[4]*Networking Research Center on Bioengineering, Biomaterials and Nanomedicine, CIBERBBN, 28029 Madrid, Spain*

[5]*The Surface Analysis Laboratory, Faculty of Engineering and Physical Sciences, University of Surrey, Guildford, GU2 4DL, UK*

[6]*Department of Mechanical Engineering, Khalifa University of Science and Technology, Abu Dhabi, P.O. Box 127788, UAE*

*Corresponding author.

Present address:

Western Macedonia University of Applied Sciences,

School of Technological Applications,

Department of Environmental and Pollution Control Engineering,

Laboratory of Alternative Fuels and Environmental Catalysis (LAFEC),

GR – 50100, Koila, Kozani, Greece

Tel: +302461068296, Fax: +302461039682

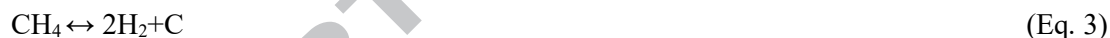E-mail address: mgoula@teiwm.gr (M.A. Goula)

ABSTRACT

Ni/Al_2O_3 and $Ni/La_2O-Al_2O_3$ catalysts were investigated for the biogas reforming reaction using CH_4/CO_2 mixtures with minimal dilution. Stability tests at various reaction temperatures were conducted and TGA/DTG, Raman, STEM-HAADF, HR-TEM, XPS techniques were used to characterize the spent samples. Graphitized carbon allotrope structures, carbon nanotubes (CNTs) and amorphous carbon were formed on all samples. Metallic Ni^0 was recorded for all (XPS), whereas a strong peak corresponding to $Ni_2O_3/NiAl_2O_4$, was observed for the Ni/Al sample (650–750°C). Stability tests confirm that the Ni/LaAl catalyst deactivates at a more gradual rate and is more active and selective in comparison to the Ni/Al for all temperatures. The Ni/LaAl exhibits good durability in terms of conversion and selectivity, whereas the Ni/Al gradually loses its activity in CH_4 and CO_2 conversion, with a concomitant decrease of the H_2 and CO yield. It can be concluded that doping Al_2O_3 with La_2O_3 stabilizes the catalyst by (a) maintaining the Ni^0 phase during the reaction, due to higher dispersion and stronger active phase-support interactions, (b) leading to a less graphitic and more defective type of deposited carbon and (c) facilitating the deposited carbon gasification due to the enhanced CO_2 adsorption on its increased surface basic sites.

Keywords: biogas reforming reaction, syngas production, nickel catalysts, catalytic deactivation, carbon nanotubes, lanthana doping

1. INTRODUCTION

It is well understood that human activities, emanating from current practices relating to the production and consumption of fossil based energy have an unequivocal impact upon the global climate. The anxiety caused by this realization, alongside the finite nature of the resources and issues relating to accessibility and affordability, have driven the development of renewable energy sources. A promising technology is the Dry Reforming of Methane (DRM), especially when biogas is used as the feedstock. Biogas is produced by the anaerobic digestion or fermentation of organic matter due to microbiological action of bacteria, and contains mainly CH_4 and CO_2 with trace amounts of H_2S, NH_3 and water vapor [1,2]. Thus, the process makes use of the main greenhouse gases and can provide a renewable resource with a potential zero carbon footprint. The product of this process is syngas, a key chemical feedstock for the synthesis of oxygenated chemicals and hydrocarbons from Fisher – Tropsch synthesis [3,4].

DRM (Eq. 1) is a highly endothermic reaction (ΔH^o_{298}=+247 kJ/mol), which is influenced by the simultaneous occurrence of the Reverse Water Gas Shift reaction (RWGS, Eq. 2) and results in a syngas ratio lower than unity [5,6]. Carbon deposition is induced by the occurrence of methane decomposition (or methane cracking, Eq. 3) and carbon monoxide disproportionation (or Boudouard reaction, Eq. 4). However, part of the carbon deposited upon the catalytic surface can be removed as CO or CO_2 via gasification (Eq. 5) or oxidation reactions (Eqs. 6 and 7). The CO methanation reaction (Eq. 8) may also be considered in the puzzle of the dry reforming of methane reactions network [7,8].

$$CH_4 + CO_2 \leftrightarrow 2CO + 2H_2 \qquad\qquad\qquad (Eq. 1)$$
$$CO_2 + H_2 \leftrightarrow CO + H_2O \qquad\qquad\qquad (Eq. 2)$$
$$CH_4 \leftrightarrow 2H_2 + C \qquad\qquad\qquad (Eq. 3)$$
$$2CO \leftrightarrow CO_2 + C \qquad\qquad\qquad (Eq. 4)$$
$$C + H_2O \leftrightarrow CO + H_2 \qquad\qquad\qquad (Eq. 5)$$
$$C + (1/2)O_2 \rightarrow CO \qquad\qquad\qquad (Eq. 6)$$
$$C + O_2 \rightarrow CO_2 \qquad\qquad\qquad (Eq. 7)$$
$$CO + 3H_2 \leftrightarrow CH_4 + H_2O \qquad\qquad\qquad (Eq. 8)$$

Noble metals such as Rh, Ru, Pd, Ir and Pt have been successfully tested in the DRM [9,10] however, their high cost and limited availability makes their use unattractive for industrial applications [11,12]. Thus, research efforts are directed towards transition metals (Fe, Co, Ni, etc), with nickel attracting considerable attention, as it is known to offer exceptional activity, especially if the Ni is highly dispersed on to the support [13,14]. However, nickel based systems are also known to suffer from deactivation due to carbon formation [15,16] and metal particle sintering due to a lack of adequate thermal stability

[17,18]. Apart from a loss of dispersion (which is detrimental to catalytic activity), sintering further aggravates carbon deposition, as large metal ensembles stimulate coke formation [19,20].

The carbonaceous species deposited upon the catalytic system differ in nature and structure depending on reaction temperature and the gas feed composition, but literature reports suggest the formation of amorphous and filamentous carbon (such as carbon nanofibers - CNFs and carbon nanotubes - CNTs) [21,22]. Often the nickel particles are found encapsulated within graphite layers, which leads to the loss of active metal sites hence reduced catalytic activity. Alternatively, carbon filament formation (whiskers) can push Ni particles on to the filament top without the expected deactivation of the Ni surface. However, whisker formation should be avoided as it leads to a blockage of the support's porosity and catalyst breakdown, whereas extensive whiskers growth can expand the catalyst bed and plug the reactor. Moreover, as Ni is placed on the filament top, it is difficult to regenerate the catalytic system because the contact between metal and support is lost [23,24]. This deteriorates the attrition resistance of the catalyst and limits its applicability in fluidized catalytic reactors.

It is generally accepted that catalytic activity depends on the nature of the support, active phase precursor, synthesis method and pretreatment [25,26]. Therefore oxides such as Al_2O_3, SiO_2, La_2O_3, CeO_2 and ZrO_2 have been used as supports for Ni based catalysts [e.g., 27-29], and transition metals (e.g., Fe, Co, Sn) [30,31], noble metals (eg., Ag, Pt, Pd) [32,33], lanthanide metals (e.g., La, Ce, Pr) [7,34] or alkaline earth metals (e.g., Sr, Ca, Ba) [35,36] have been used as additives in the supports to induce support-mediated promotional effects on the catalytic system. Rezaei et al. [37] reported on the effects of K_2O promoter on the activity, stability, and coke deposition of Ni catalysts supported on mesoporous nanocrystalline zirconia powder with high surface area and pure tetragonal crystallite phase. The authors reported that the addition of K_2O promoter affected the catalyst structure, increased the activity and stability, and also reduced the coke deposition on the catalysts. Alvara and Rezaei used mesoporous nanocrystalline $MgAl_2O_4$ spinel powders with high surface area and the results showed that the synthesized powders could be considered promising as supports for nickel catalysts [38]. Alipour et al. [39] used MgO-modified Ni/Al_2O_3 catalysts with different Ni loadings and investigated the effect of Ni loadings on the activity and coke formation of $Ni/MgO-Al_2O_3$ catalysts. The results obtained showed that increasing nickel loading decreased the BET surface area and increased the catalytic activity and amount of deposited carbon. Nanostructured Co–MgO mixed oxide catalysts with different cobalt contents have also been used by Mirzaei et al. [40]. BET analysis showed a high specific surface area and mesoporous structure (pore sizes < 15 nm) and TEM analysis indicated a nanostructure with crystallite sizes smaller than 10 nm for the prepared catalysts. The results obtained revealed that the catalyst with cobalt content of 10 wt.% had the highest activity and stability. However, searching through the available literature it becomes clear that alumina has been the most widely used catalyst support in the DRM due to its high

specific area (which improves metal dispersion) and its mechanical and chemical resistance under reaction conditions. The drawback of using alumina is that it also induces the deposition of carbon [41,42].

In a previous study carried out by our group [43] using a lanthana modified commercial alumina support (MI 386 fromW.R. Grace), we confirmed that the basic character of lanthanum oxide (La_2O_3) has promotional effects for nickel based catalysts in the DRM. In separate work [44] we also argued that the modification of alumina with lanthana facilitates the dispersion of active species, strengthens the interactions between nickel species and support, increases the population of basic sites, and helps redistribute the acid sites in terms of strength and density. Promotional effects induced by the incorporation of lanthana into the alumina support have also been reported by other researchers. For example, Martinez et al. [45] argued that an increase in Ni dispersion in samples containing La leads to more metallic particles with diameters less than 10 nm that contribute to the catalytic conversion without producing large amounts of coke in filaments. Liu et al. [46] reported that the improved performance of nickel supported on lanthana-alumina catalysts with a La/Al ratio equal to 0.05 resulted at highly dispersed La species on the catalytic surface. Moreover, Slagtern et al. [47] reported that when lanthana is used in the support of DRM catalysts, CO_2 is activated by La_2O_3 through the formation of $La_2O_2CO_3$, which can eliminate the deposited carbon at the $Ni-La_2O_3$ interface by means of promoting coke oxidation.

Despite all previous efforts, biogas dry reforming is not as yet an industrially mature process in large part due to the operational constraints exhibited by the various catalysts involved. As several studies have shown, satisfactory catalytic activity and stability are dictated in large part by active metal dispersion, adhesion to support and resistance to sintering, but also by low carbon formation. While a good catalyst cannot fully eliminate the formation of coke, it can favor the formation of more reactive intermediate carbonaceous species. It is further desirable to tackle the issue of catalyst design based on an understanding of its deactivation mechanism. For this purpose, an in depth analysis of the spent catalysts' surface at various reaction temperatures by employing surface analysis techniques would be very useful, as the number of publications that include all these techniques is rather limited.

Prompted by the above, we further expanded our studies on Ni/Al and Ni/LaAl catalysts using CH_4/CO_2 mixtures with minimal dilution (as found in commercial applications in biogas utilization processes), and focused on investigating the correlation between catalytic deactivation and quantity and/or quality of deposited carbon, as a function of the applied conditions. To this purpose, we have conducted a number of stability tests at different reaction temperatures (600, 650, 700, 750, 800°C) and employed various techniques such as Thermogravimetric analysis (TGA/DTG), Raman spectroscopy, Transmission Electron Microscopy (STEM-HAADF and HR-TEM) and X-ray Photoelectron Spectroscopy (XPS) in

order to characterize the coke deposited on the spent catalytic samples and also to monitor the evolution of Ni oxidation states with the reaction conditions.

2. EXPERIMENTAL

2.1 Catalyst preparation and characterization

The properties of the commercially available alumina (Akzo) and lanthanum-alumina (4 wt. % La_2O_3, W.R. Grace, MI-386) supports used herein, as well as details over the preparation method of the Ni catalysts, can be found in [43,44]. In short, the supports were sieved to 350-500 μm and calcined at 800°C for 4 h. The catalysts were prepared via the wet impregnation technique using a 0.17 M $Ni(NO_3)_2 6H_2O$ (Sigma Aldrich) aqueous solution to give catalysts with a Ni content of 8 wt. %. The water was evaporated from the slurries under continuous stirring at 75°C for 5h and the suspensions were dried at 120°C for 12 h and calcined in air at 800°C for 4 h; these samples are denoted in this manuscript as "calcined" catalysts. For catalytic evaluation studies the samples were in-situ activated for 1 h at 800°C under pure H_2 flow and are denoted herein as "reduced" catalysts.

Detailed information regarding the characterization of catalytic samples prior to testing (i.e., calcined and/or reduced samples) have been already reported in [43,44]. In short: (i) total metal loading was determined by Inductively Coupled Plasma Atomic Emission Spectroscopy (ICP-AES), (ii) Specific Surface Area was estimated using N_2 adsorption/desorption and the multi-point Brunauer-Emmet-Teller (BET) method, (iii) crystalline structure was determined by powder X-ray diffraction (PXRD), (iv) redox properties were measured by temperature programmed reduction (H_2-TPR), and (v) surface acidity-bacidity was estimated by temperature programmed desorption (CO_2-TPD and NH_3-TPD). For the supports, the Point of Zero Charge (PZC) was determined using potentiometric Mass Titrations (PMTs), and XRD, BET and H_2-TPR measurements were also performed.

The amount of carbon deposited on the catalysts presented herein was measured with a thermogravimetric analyzer (TGA), on a Leco TGA701 instrument. The thermal decomposition process of the coke formed onto the spent catalysts was also obtained. In the procedure, ≈50 mg of the spent catalyst was subjected to TGA scan from room temperature (RT) to 1000°C at a heating rate of 10°C min^{-1} under a flow of dry air (3.5 L min^{-1}). Curie point standards were utilized for the temperature calibration.

The coke deposited on the spent catalytic samples was also characterized by Raman spectroscopy. Spectra were collected using a WITEC alpha300R micro-Raman system (RAMAN Imaging System WITEC alpha300R) with a 20× long distance objective (0.35 numerical aperture) in the back-scattering geometry with an excitation wavelength of 532 nm from an Ar$^+$ ion laser (laser power set at 2 mW calibrated against a silicon standard). For each sample, at least three Raman spectra were collected in different areas to assess the homogeneity of the investigated material.

Transmission electron microscopy (TEM) measurement on the reduced and spent catalysts was carried out using a 200 kV G2 20 S-Twin Tecnai microscope with a LaB6 electron source fitted with a "SuperTwin®" objective lens allowing a point to point resolution of 0.24 nm. Energy dispersive X-ray spectroscopy (EDS) and high angle annular dark field scanning transmission electron microscopy (STEM-HAADF) were performed on a Tecnai G2-F30 Field Emission Gun microscope with a super-twin lens and 0.2 nm point-to-point resolution and 0.1 nm line resolution operated at 300 kV. The HAADF detector enables the acquisition of STEM-HAADF images with atomic number contrast for high scattering angles of the electrons (Z-contrast). To prepare the samples for transmission electron microscopy studies, the catalyst powder was dispersed in milli-Q water. After 30 s in an ultrasonic bath, a drop of this suspension was applied to a copper grid (200 mesh) coated with carbon film, and allowed to dry in air. High Resolution TEM (HR-TEM) observations were carried out using a FEI TITAN^3 image corrected (60−300 kV) TEM operated at 300 kV. To prepare the sample, the nanoparticle suspension was diluted with ethanol and sonicated for 30 s before casting 5 μL on a carbon TEM grid.

XPS analyses of the spent catalytic samples presented herein were performed on a ThermoFisher Scientific Instruments (East Grinstead, UK) K-Alpha+ spectrometer. XPS spectra were acquired using a monochromated Al Kα X-ray source (hν = 1486.6 eV). An X-ray spot of ~400 μm radius was employed. Survey spectra were acquired employing a Pass Energy of 200 eV. High resolution, core level spectra for all elements were acquired with a Pass Energy of 50 eV. Quantitative surface chemical analyses were calculated from the high resolution, core level spectra following the removal of a non-linear (Shirley) background. The manufacturers Avantage software was used, which incorporates the appropriate sensitivity factors and corrects for the electron energy analyzer transmission function.

2.2 Catalytic tests

The catalytic tests were performed at atmospheric pressure, using a continuous flow, stainless steel, fixed bed, tubular reactor. The gas mixture used as feed in the reactor inlet consisted of 55% CH_4, 35% CO_2 and 10% Ar, corresponding to a CH_4/CO_2 molar ratio equal to 1.56. The experimental protocol used was designed in order to thoroughly investigate carbon deposition during the DRM reaction using reaction temperature and time-on-stream as variables. Thus, the progress of the DRM reaction (and carbon deposition) was investigated during short constant time-on-stream tests of 10 h at a constant WHSV equal to 40,000 mL g^{-1} h^{-1} (total flow rate was 100 mL min^{-1} and the catalyst weight 150 mg). The catalyst pre-condition procedure involved in situ activation under a pure hydrogen flow (100 mL min^{-1}) at $800^{\circ}C$ for 1 h. After the reduction procedure, the reactor was returned to the temperature of interest under He flow (100 mL min^{-1}).

Reactants and products were analyzed by on-line gas chromatography in a CG-Agilent 7890A gas chromatograph, with two columns in parallel, HP-Plot-Q (19095-Q04, 30 m length, 0.530 mm I.D.) and HP-Molesieve (19095P-MSO, 30 m length, 0.530 mm I.D.), equipped with TCD and FID detectors.

The CH_4 or CO_2 conversions and H_2 or CO yields were calculated by Eqs. (9), (10), (11) and (12), respectively:

$$X_{CH_4}(\%) = \frac{F_{CH_4,in} - F_{CH_4,out}}{F_{CH_4,in}} \times 100 \qquad \text{(Eq. 9)}$$

$$X_{CO_2}(\%) = \frac{F_{CO_2,in} - F_{CO_2,out}}{F_{CO_2,in}} \times 100 \qquad \text{(Eq. 10)}$$

$$Y_{H_2}(\%) = \frac{F_{H_2}}{2F_{CH_4,in}} \times 100 \qquad \text{(Eq. 11)}$$

$$Y_{CO}(\%) = \frac{F_{CO}}{F_{CH_4,in} + F_{CO_2,in}} \times 100 \qquad \text{(Eq. 12)}$$

where $F_{i,in}$ or $F_{i,out}$ is the flow rate of the component i in feed or effluent gas mixture.

3. RESULTS AND DISCUSSION

3.1 Characterization results for fresh catalysts

As mentioned above, the Ni/Al and Ni/LaAl catalysts in their calcined and/or their reduced form were characterized by N_2 adsorption/desorption, ICP, XRD, NH_3-TPD, CO_2-TPD and H_2-TPR, while the calcined supports were characterized by PZC/PMT, XRD, BET and H_2-TPR. The main findings of these characterization techniques will be summarized in this section, as they will be used below in explaining catalytic performance and/or carbon deposition; a detailed discussion can be found in [**43,44**].

Regarding the supports, the determination of the Point of Zero Charge (PZC) confirmed the increased basic characteristics of LaAl (6.8 and 10.0 for the Al and LaAl, respectively), but XRD diffractograms, apart from showing the characteristic features of γ-Al_2O_3, failed to detect the La_2O_3 phase (indicating either high dispersion or an amorphous structure) and H_2-TPR measurements revealed that neither of the supports had significant oxygen storage capacity (OSC) values.

In regards to the reduced catalytic samples, measurements of metal loading by ICP showed comparable values for both samples (7.14 and 7.79 wt. % for the Ni/Al and Ni/LaAl, respectively). Further, the two samples also revealed similar specific surface areas (136 and 126 m^2g^{-1}), average pore diameters (20.1 and 21.1 nm) and N_2 adsorption-desorption isotherms of Type IV(a), which are typical of mesoporous

material with some macroporosity. However, the Ni/Al catalyst showed an H2(b) type hysteresis loop and the Ni/LaAl an H3 type hysteresis loop, while pore size distribution curves showed that for the Ni/Al sample, the majority of the population of pores were in the meso-range and the Ni/LaAl catalyst contained mainly meso, but also some macropores. Apart from γ-Al_2O_3, the XRD diffractograms of the reduced catalysts showed the formation of $NiAl_2O_4$ (attributed to the high calcination temperature), and the presence of low intensity peaks of metallic nickel, indicating the small size of the Ni particulates. As a number of recent works have shown the presence of nickel aluminate spinel can improve catalyst resistance to carbon deposition [48-50]. Moreover, Ni^0 dispersion for the Ni/LaAl catalyst was almost 2.5 times higher in comparison to the Ni/Al, which was attributed to the presence of La_2O_3 in the support. In addition, measurements regarding surface acidity-basicity showed an increase in the basic sites population (CO_2-TPD) and a redistribution of the acid sites in terms of strength and density (NH_3-TPD) for the Ni/LaAl catalyst. Moreover, the TPR results for the same catalyst showed strengthened metal-support interaction, as the reduction temperatures of the nickel species that are embedded in Ni–Al skeleton and strongly interact with the alumina support migrated to higher temperatures.

Fig. 1 shows the TEM images (a,b), the particle size distribution histogram (d), STEM-HAADF images (e,f), and the EDS spectra (g) for the Ni/LaAl catalyst. It also shows the STEM-HAADF images (h), EDS spectra (i) and particle size distribution histogram (k) for the Ni/Al catalyst. Further, Fig. 1(c) and 1(j) show schematic diagrams of the catalyst structure for the Ni/LaAl and Ni/Al samples, respectively. For both catalysts the Ni^0 particles appear to be of spherical morphology and to have a relatively uniform distribution on the respective supports. TEM analysis of the size distribution for the Ni/LaAl catalyst revealed the presence of particles distributed in a narrow range (5–16 nm) with a mean size of 10.3 nm (standard deviation, SD = 2.2nm), while for the Ni/Al sample the particles were distributed between 5-28 nm with a mean size of 14.4 nm (SD = 4.5nm). Fig. 1(h) shows a Z-contrast scanning transmission electron microscopy image of Ni/Al catalyst and Ni nanoparticles (high brightness) are found homogenously distributed in the Al_2O_3 support. EDS analysis confirmed that the composition of the brighter regions was Ni (Fig. 1i).

3.1 Characterization results for spent catalysts

3.1.1 Textural characterization

Fig. 2 presents N_2 adsorption/desorption isotherms and the pore size distribution curves of the Ni/Al and Ni/LaAl catalysts after reduction and reaction at 600, 700 and 800°C. For the pore size distribution curves, the BJH adsorption data was used. The isotherms for all samples are type IVa with a hysteresis loop indicating the presence of mesopores. It is known that the adsorption behavior in mesopores is determined by the adsorbent-adsorptive interactions and also by the interactions between the molecules in

the condensed state. A typical feature of Type IV isotherms is a final saturation plateau, of variable length (sometimes reduced to a mere inflexion point). Especially for Type IVa isotherms, capillary condensation is accompanied by hysteresis occurring for pores wider than ~ 4 nm) [51]. The hysteresis loop for the Ni/Al reduced sample is H2(b) type, indicating the pore connectivity with ink-bottle or channel-like pores which is characteristic for mesoporous materials. After reaction this loop was progressively transformed to an H3 type, typical for materials with pore network consisting of macropores which are not completely filled with pore condensate. On the other hand, for the Ni/LaAl samples (reduced and spent) the observed hysteresis loop is H3 type as the adsorption branch resembles a Type II isotherm and the lower limit of the desorption branch is normally located at the cavitation-induced p/p^0.

The pore size distribution curves show that for the Ni/Al samples these are of single modal type in the mesopore range, centered around 10 to 20 nm (reduced and used at 800°C) with a shift to the micropore range for the sample used at 600 and 700°C. On the contrary, for the Ni/LaAl samples a bimodal pore size distribution can be observed located in the meso-and macro-pore range. More importantly, for the spent catalysts there is a shift to larger mean diameter, indicating that a pore blogging exists at the meso-range. It can be suggested that for both spent catalysts (Ni/Al and Ni/LaAl) carbon deposition that occurred at the lower reaction temperatures (600 and 700 $^{\circ}$C) covered the meso-pores' (20-40nm) internal surface. Textural properties of the reduced and spent samples (Ni/Al, Ni/LaAl) including the specific surface area, pore volume and average pore width are presented in Table 1. It can be seen that the SSA of the spent Ni/Al catalysts decreased considerably, the average pore diameter was reduced from 20 to 15nm, whereas total porosity decreased significantly (especially for 600 and 700°C reaction temperature). For the Ni/LaAl samples an analogous loss in SSA after reaction can be observed, accompanied with a more rational decrease in the pore volume (ever for the lower reaction temperatures). This observation is an indication that most of the pores are still available (little pore blockage) suggesting lower carbon deposition and as a consequence higher long term stability of the Ni/LaAl catalyst. This finding will be further corroborated upon discussing the TGA, TEM, Raman and XPS results below.

3.1.2 TGA/DTG analysis

The carbon deposited on to the catalysts tested herein was examined by TGA and the derivative thermo-gravimetric (DTG) graphs are presented in Fig. 3. As can be observed, the oxidation process appears to differ between the two samples. Specifically, for the Ni/Al spent catalyst the main thermal event is confined between 450-700°C for the samples tested at 600 and 650°C and expands up to 800°C for the samples tested at higher temperatures, i.e., the catalysts tested at 700, 750 and 800°C. In contrast, the main thermal event for the Ni/LaAl catalyst is found between 450-700°C irrespective of the temperatures under which the catalysts were tested. As is widely accepted, amorphous carbon combusts at temperatures between 200 and 500 °C, disordered structures such as carbon nanofibers (CNFs) and carbon nanotubes

(CNTs) with some defects and/or different structural arrangements are burned between 500 and 600 °C, and more graphitic structures, such as multi wall carbon nanotubes (MWCNTs) with an almost perfect graphene sheet arrangement combust between 600 and 800 °C [52,53]. Thus, the DTG graphs presented herein indicate that amorphous, filamentous carbon (CNFs and CNTs) and graphene-like structures were deposited on the catalysts during the reaction however, higher fractions of graphitic structures were deposited on the Ni/Al catalyst, especially at higher reaction temperatures, as will be confirmed when discussing the Raman results presented below. An additional observation, also indicating higher fractions of graphitic structures on to the Ni/Al catalyst, is that the rate of carbon oxidation is lower in comparison to the Ni/LaAl catalyst. This enhanced degree of graphitization of the carbon deposited on the un-promoted catalyst can most probably be attributed to its higher Ni crystallite size [44]. According to the literature amorphous and filamentous carbon deposits are better tolerated, as they are easier to remove by gasifying with O_2. On the other hand, crystalline graphite is considered as the carbon form having the most adverse effect on catalytic performance as it acts like a shell on the catalyst covering layer by layer the nickel active sites [31,54]. Thus, this initial examination indicates that the addition of La_2O_3 leads to a less graphitic type of deposited carbon, which could provide a catalyst with longer term stability.

3.1.3 Raman spectroscopy analysis

Raman spectroscopy was used to help investigate the nature and the graphitization order characteristics of the carbon deposits formed onto the spent catalysts tested herein and the results are presented in Fig. 4 (the corresponding fitting curves in the region of 800-3300 cm^{-1} are also depicted by red lines). Both samples (at all testing temperatures) show a first order region between 1000 and 2000 cm^{-1} and a second order region between 2300 and 3300 cm^{-1}. The first order region is governed by two broad bands, i.e., the G-band, which appears between 1500 and 1600 cm^{-1}, and the D-band located between 1300 and 1400 cm^{-1}. The former is related to the Raman-allowed phonon mode E_{2g} and involves out-of phase intra-layer displacement in the graphene structure, while the latter relates to polycrystalline imperfect graphite [55,56]. Another disorder-induced Raman signal, known as D′-band, can be found around 1610 cm^{-1} and appears as a shoulder of the classical G-band. The D′ mode does not exist in pure graphite, but it is observed for graphitic defects or disordered carbons [57,58]. In the second-order region of the spectra, between 2300 cm^{-1} and 3300 cm^{-1}, three main bands can be observed for the spent catalysts tested herein, i.e., the D″ (2435 cm^{-1}), 2D (2675 cm^{-1}) and G+D (2900 cm^{-1}). These correspond to overtones and combinations of the bands coming from the first order region. Specifically, the D″ band can be attributed to the Raman-active first overtone of a Raman-inactive graphitic lattice vibration mode at ~1220 cm^{-1}, while the other two bands are also found in the spectrum of crystalline graphite and graphene. The most intense one is positioned around 2700 cm^{-1} (2D) and is typically found in graphite spectrums [59,60].

The deconvolution of the Raman spectra in all samples revealed that the G and D-band peaks were centered at 1565 and 1345 cm^{-1} and according to the literature [61,62], these peaks are characteristic of CNTs. The degree of crystallinity of the carbon formed during the biogas dry reforming reaction can also be gauged by the relative intensity of the D and G-bands (I_D/I_G), as smaller I_D/I_G values indicate higher crystallinity due to higher contribution of the graphitized carbon formed [63,64]. For the catalysts tested herein, it is clear that the degree of crystallinity increases with an increase of the reaction temperature however, it is significantly more pronounced for the Ni/Al catalyst. Specifically, the I_D/I_G ratio for the Ni/Al sample follows the order 1.32> 0.72> 0.45> 0.44> 0.35 and for the Ni/LaAl 1.42> 1.18> 1.06> 0.98> 0.86 at 600, 650, 700, 750 and 800°C, respectively. Thus, the Raman spectra for the Ni/Al and Ni/LaAl catalysts confirm the formation of different carbon structures on the used catalysts and hint that the fraction of different carbon types depends on the catalyst-support nature. Moreover, carbon deposition on the Ni/Al catalyst seems to mainly occur on the Ni surface leading to growth of graphitic carbon, which is mostly responsible for deactivation, as it acts like a shell covering the Ni active sites layer by layer.

3.1.4 Electron microscopy analysis

Fig. 5 show the TEM images of Ni/Al (a,b) and Ni/LaAl (c,d) spent catalysts, at 600 and 800°C, respectively. At 600°C (Fig 5a and c), both samples exhibit a tendency to form crystalline carbon allotrope structures in the shape of carbon nanotubes, as well as co-existent amorphous carbon (indicated by arrows and dashed circles). In both cases also the encapsulated Ni particles are depicted by red dashed circles. At 800 °C, amorphous carbon is absent on the Ni/Al catalyst (Fig. 5b) and encapsulated catalytic metallic nanoparticles can be observed. On the other hand, amorphous carbon can be observed on the modified system even at 800°C (Fig 5d) and as mentioned previously, this type of carbon can be more easily combusted during the catalytic reaction [16,65]. Moreover, at 800°C, the Ni/Al catalyst showed also the interesting finding of core-shell carbon coated nickel nanoparticles (16 graphitic sheets in the shell, Fig. 5b) that together with the highly graphitized CNTs formed, explain the excellent I_D/I_G ratios found by Raman spectroscopy. Fig. 6 shows the high resolution TEM (HR-TEM) images of Ni/Al (Fig. 6a) and Ni/LaAl (Fig. 6b) used catalysts at 800°C. From the Raman spectra, both samples were expected to depict crystalline structures of carbon materials and the shape of Raman signals was associated with the specific morphology and geometry of multi-walled carbon nanotubes, as discussed previously. The morphology of the carbon deposits demonstrated by the HR-TEM images shows clearly a multitude of defects on the CNTs formed onto the Ni/LaAl system. These defects (depicted by red dashed circles) could be attributed to oxygen transferred and inserted in the graphitic lattice during CNT growth, which

inhibits the formation of CNTs with continuous, straight walls [**66**] and are important as they are the favored sites of attack by oxidizing gases [**52,60**].

3.1.5 XPS analysis

Fig. 7a presents the Ni2p core level spectra of the NiAl catalyst following the catalytic reaction at different conditions in the 600-800 ^{o}C temperature range for 10h, aiming to monitor the evolution of Ni oxidation states with the reaction conditions. Table 1 gives the XPS peak binding energies and elemental surface concentrations for the same catalyst. Firstly, it should be noted that the Ni concentrations are below 0.5 at.% for all samples, due to the high concentrations of C, O and to a lesser extent Al. A low binding energy component corresponding to metallic Ni^0 at around 853.0 eV can be observed in many of the Ni 2p spectra recorded at the different temperatures. However, a stronger peak, observed for temperatures 650–750°C occurs at a binding energy of 856.5-857.0 eV, corresponding to $Ni_2O_3/NiAl_2O_4$ [**67**]. The carbon concentration on the surface, was found to be >90 at.% following the reaction at 600°C, and this high amount of carbon drops as the reaction temperature is elevated (Table 1). This can be attributed to an enhancement of carbon gasification reaction at higher temperatures, in addition to the inability of the Boudouard reaction occurring at these temperatures.

Fig. 7b presents the Ni2p core level spectra for the Ni/LaAl catalyst. Firstly, it should be noted that the Ni 2p region overlaps with the La $3d_{3/2}$ peak, which prevents any clear detailed interpretation. However, the Ni 2p peak shape and associated satellite structure is similar in many cases to that observed for the Ni/Al catalyst. Furthermore, despite the same Ni loading in the two catalysts herein, the La-modified catalyst exhibits higher surface Ni concentration compared to the La-free catalyst (Table 2). This is in agreement with the literature, where La, Ca and Mg addition as support modifiers have been reported to improve Ni dispersion [**44,68,69**]. Also, as the temperature of reaction increases to 800°C, the relative concentration of Ni^0 compared to oxidized Ni is increased. When La is added to the catalyst the carbon contamination at 600°C is lower (compared to the Ni/Al catalyst) and the drop of surface carbon as the temperature is raised is even more pronounced than before (Ni/Al catalyst case). This is in agreement with the fact that basic oxides favor carbon gasification reactions [**70,71**].

The C 1s peaks for all spent catalytic samples (Figs. 8a and 8b) exhibited a peak shape typical of sp^2 hybridised carbon, confirmed by the D-parameter value (derived from the first derivative of the C KLL Auger peak in the XPS spectrum) [**72**] being 19.6 – 20.4 in all cases. These results are in accordance with the literature, as it has been reported that the carbon deposition can be significantly suppressed due to the interaction between Ni particles and lanthana species in Ni based Al_2O_3 catalyst modified by La_2O_3 [**44,73**].

3.2 Catalytic stability

The catalytic stability test results (10 hrs time-on-stream) for the Ni/Al and Ni/LaAl samples were conducted at five (5) different reaction temperatures (600, 650, 700, 750, 800°C), using a fresh catalytic sample for each experiment. The variations in the values of CH_4 and CO_2 during reaction conversion (X_{CH4} and X_{CO2}) are depicted in Fig. 9, H_2 and CO yield (Y_{H2}, Y_{CO}) in Fig. 10 and H_2/CO molar ratio in Fig. 11. For the Ni/Al sample a sharp drop in the conversion and yield values can be observed for the first two hours of the reaction (except for the reaction at 800°C), leading to a loss of about half of its initial activity. On the other hand, the Ni/LaAl sample seems to deactivate at a more gradual rate and it appears to be more active and selective compared to the Ni/Al catalyst for all reaction temperatures. The differences between the catalysts seems to be more pronounced at T=750°C, in which temperature the Ni/LaAl catalyst has almost twice the values for both X_{CH4} (58.5%) and Y_{H2} (60%) in comparison to the Ni/Al. It is noted that CH_4 and CO_2 conversion at all reaction temperatures for the Ni/LaAl catalyst are close to those predicted by thermodynamics [74].

Moreover, for both catalysts there is a decreasing trend to their final activity loss (after 10 hrs time-on-stream) with an increase of the reaction temperature. Specifically, their activity loss ($\Delta X_{(CH4)}\%$) ranges from 70% (600°C) to 20% (800°C) for the Ni/Al and from 40% (600°C) to 10% (800°C) for the Ni/LaAl. Since the values X_{CO2}, Y_{H2}, Y_{CO} can be influenced by the RWGS reaction, it can be said that only the X_{CH4} stands as a true measure of the DRM activity. As for the H_2/CO molar ratio its values are almost constant in the time interval of the 10 h examined, except at the first 2h of operation in which elevated H_2/CO values (up to 1) have been recorded. Elevated H_2/CO values imply pronounced occurrence of the methane cracking reaction (Eq. 3) and/or Boudouard reaction (Eq. 4), which are the main reactions responsible for carbon deposition [**74**].

Obviously, the catalytic behavior of Ni/LaAl and Ni/Al strongly differs in terms of stability. The Ni/LaAl exhibits a good durability in terms of conversion and selectivity, whereas Ni/Al gradually loses its activity in CH_4 and CO_2 conversion with a concomitant decrease of the H_2 and CO yield. It should be mentioned here that catalysts undergo significant deactivation, due to the extremely severe experimental conditions that were applied, as an almost undiluted feed with a high CH_4 to CO_2 ratio (equal to 1.56) and WHSV equal to 40,000 mL g^{-1} h^{-1} were used for the time-on-stream experiments.

The improved catalytic performance, concerning activity and H_2 production of the Ni/LaAl sample can be attributed to the higher active phase (Ni^0) surface concentration, as was evidenced by the XPS analysis results. It can be said that the modification of alumina with lanthana not only facilitates the active species dispersion and strengthens the interactions between Ni species and support, but also stabilizes the catalyst by maintaining the metallic nickel phase during the reaction. Furthermore, the increase in the population

of basic sites contributes to catalyst's stability, by facilitating the deposited carbon gasification due to the enhanced CO_2 adsorption on its surface.

3.3 Correlation between deactivation and the carbon deposited on the surface

According to the literature, catalytic stability during DRM gets affected mainly by coking, but also depends on particle sintering, together with re-oxidation and hydroxylation of active species [54,75-77]. As discussed previously, carbon formation can occur through methane decomposition (Eq. 3), the Boudouard reaction (Eq. 4) and possibly, carbon monoxide hydrogenation ($C+H_2O \leftrightarrow CO+H_2$). Methane decomposition, as an endothermic reaction, is the key reaction for carbon deposition for feeds with CH_4/CO_2 higher than unity, as in our case, leading to increased H_2 production and solid carbon deposition, even at high temperatures. In the temperature range of 550-675°C, the deposited coke can be produced via all coke forming reactions and as a result, it is the region where extensive coke formation can be expected [74].

As mentioned above, the Ni/Al catalyst exhibits lower activity with time-on-stream, while the Ni/LaAl appears quite durable in terms of conversion and selectivity. This was somewhat expected as higher fractions of graphitic structures, considered to be difficult to oxidize, were deposited on the Ni/Al catalyst (TGA/DTG and Raman results). Moreover, with the presence of La_2O_3 on the catalytic surface, the carbon that was detected by XPS analysis on the used catalysts was lower for all reaction temperatures and the drop of surface carbon as the temperature was raised was even more pronounced than for the Ni/Al catalyst. More importantly, the existence of Ni in the Ni^0 metal state for the Ni/LaAl catalyst is crucial in ensuring that the O species could react with the accumulated carbon on the Ni crystallites to produce CO, in order to prevent coverage of Ni crystallites with carbon [29]. It can be said that the stabilization of well-dispersed Ni^0 within the alumina matrix is the key factor accounting for the significant long-term performance of the Ni/LaAl sample, in spite of the harsh experimental conditions (non-diluted feed) employed for the biogas reforming reaction [78]. Moreover, as presented at Table 1, both catalysts seem to be quite resistant to sintering, as the Ni^0 mean crystallite size does not seem to change significantly between the reduced and the spent samples.

The above findings are in accordance with the literature, as it has been reported that promoters such as La_2O_3 increase both the dispersion and the reducibility of the Ni supported catalysts [45,46,68]. Specifically, La aids in the removal of the carbon deposits more effectively by gasification, preventing catalytic deactivation that is caused by insufficient removal of carbon species from the surface of Ni particles and the formation of stable, graphitic carbon deposits, most likely covering the surface of metal [79,80].

In view of the high carbon contents in the spent Ni/Al samples (Table 1), such coke deposits are considered to be formed at a significant extent in the less basic alumina-based materials [81,82]. This can be interpreted in term of a faster overall process of CH_4 decomposition and carbon polymerization compared to CO_2 activation. On the contrary, the rates of carbon formation and gasification reactions seem to be of the same order on more basic Ni/LaAl catalysts. Even when carbon exists at a significant amount (Table 2), the coke deposits are present as nanotubes grown on few external isolated Ni^0 nanoparticles located at the surface of the alumina grains (Fig.6b). As a result, they are not detrimental to catalytic stability because they remain outside the pores, far away from the Ni^0 nanoparticles that are kept occluded inside the pores, so are still accessible and active towards the reactants [83].

The different catalytic performance that was observed for the Ni/Al and Ni/LaAl catalysts could be interpreted by the specific reaction mechanism that has been proposed for the methane dry reforming reaction over Ni/La$_2$O$_3$ catalysts. In fact, it was suggested that CH_4 activation and dissociation take place on the surface of Ni particles to form H_2 and active carbon intermediate species [84]. On the other hand, CO_2 adsorbs on La_2O_3 to form $La_2O_2CO_3$ which can react with neighboring active carbonaceous intermediate species to produce CO and regenerate La_2O_3, completing the cycle between $La_2O_2CO_3$ and La_2O_3. It should be also noticed that $La_2O_2CO_3$ formed during reaction process may react with coke on the interface between nearby Ni particles and support [85,86].

4. CONCLUSIONS

In the present work, the biogas dry reforming reaction for Ni/Al and Ni/LaAl catalysts was investigated using CH_4/CO_2 mixtures with minimal dilution. The work focuses on the correlation between deactivation and the quantity and/or quality of the deposited carbon. Stability tests at various reaction temperatures were conducted and techniques such as TGA/DTG, Raman, STEM-HAADF, HR-TEM and XPS were employed in order to characterize the coke deposited on the spent samples and to monitor the evolution of Ni oxidation states with the reaction conditions. From TGA/DTG and Raman results it was found that the degree of carbon crystallinity increases with increasing the reaction temperature, whereas the addition of La_2O_3 leads to a less graphitic type of deposited carbon, which could actually provide a catalyst with longer term stability. TEM analysis revealed that both samples exhibit a tendency to form graphitized carbon allotrope structures in the shape of carbon nanotubes, as well as co-existent amorphous carbon. The morphology of the carbon deposits demonstrated by the HR-TEM images showed clearly the defects of the CNTs formed onto the spent Ni/LaAl catalyst.

From the XPS results it was noticed that the surface Ni concentrations was below 0.5 at.% for all cases, but the La-modified catalyst exhibited higher values compared to the un-modified sample. The carbon concentration on the surface was found to be >90 at.% following the reaction at 600°C, but this high

amount of carbon dropped as the temperature was elevated. For all samples, metallic Ni^0 was recorded, but a stronger peak corresponding to $Ni_2O_3/NiAl_2O_4$ was observed for the Ni/Al (650–750°C); as the temperature of reaction increased up to 800°C the relative concentration of Ni^0 compared to oxidized Ni increased. For the Ni/LaAl sample, carbon deposition at 600°C was lower (compared to the Ni/Al) and the drop of surface carbon as the temperature increased, was even more pronounced than before (Ni/Al catalyst case).

Stability tests confirmed that the Ni/LaAl sample deactivated at a more gradual rate and was more active and selective in comparison to the Ni/Al for all reaction temperatures. Specifically, the Ni/LaAl exhibited good durability in terms of conversion and selectivity, whereas the Ni/Al gradually lost its activity in CH_4 and CO_2 conversion with a concomitant decrease of the H_2 and CO yield. It can be concluded that the doping of Al_2O_3 with La_2O_3 stabilized the catalyst by: (a) maintaining the Ni^0 phase during the reaction, due to higher dispersion and stronger active phase-support interactions and (b) facilitating the deposited carbon gasification due to the enhanced CO_2 adsorption on its increased surface basic sites. As a result, higher fractions of graphitic structures, considered to be more difficult to oxidize, were deposited on the Ni/Al catalyst. More importantly, the existence of Ni in the Ni^0 metal state for the Ni/LaAl catalyst seems to be crucial in ensuring that the O species could react with the accumulated carbon on the Ni crystallites to produce CO, in order to prevent coverage of Ni crystallites with carbon.

ACKNOWLEDGEMENTS

REFERENCES

1.	S. Ahmed, M. Kazda, Anaerobic co-digestion process for biogas production: Progress, challenges and perspectives, Renew. Sust. Energ. Rev. 76 (2017) 1485-1496.

2.	N.D. Charisiou, A. Baklavaridis, V.G. Papadakis, M.A. Goula, Synthesis gas production via the biogas reforming reaction over $Ni/MgO–Al_2O_3$ and $Ni/CaO–Al_2O_3$ catalysts, Waste Biomass Valori. 7 (2016) 1020-1027.

3.	P. Ugarte, P. Duran, J. Lasobras, J. Soler, M. Memendez, J. Herguido, Dry reforming of biogas in fluidized bed: Process intensification, Int. J. Hydrogen Energ. 42 (2017) 13589-13597.

4.   R. Rana, C. Ingrao, M. Lombardi, C. Tricase, Greenhouse gas emissions of an agro-biogas energy system: Estimation under the Renewable Energy Directive, Sci. Total Environ. 550 (2016) 1182-1195.

5.   M. Usman, W.M.A. Wan Daud, H.F. Abbas, Dry reforming of methane: Influence of process parameters—A review, Renew. Sust. Energ. Rev. 45 (2015) 710-744.

6.   D.G. Avraam, T.I. Halkides, D.K. Liguras, O.A. Bereketidou, M.A. Goula, An experimental and theoretical approach for the biogas steam reforming reaction, Int. J. Hydrogen Energ. 35 (2010) 9818-9827.

7.   M.A. Vasiliades, M.M. Makri, P. Djinovic, B. Erjavec, A. Pintar, A.M. Efstathiou, Dry reforming of methane over 5wt% $Ni/Ce_{1-x}Pr_xO_{2-\delta}$ catalysts: Performance and characterisation of active and inactive carbon by transient isotopic techniques, Appl. Catal. B 197 (2016) 168-183.

8.   M.A. Munoz, J.J. Calvino, J.M. Rodriguez-Izquierdo, G. Blanco, D.C. Arias, J.A. Perez-Omil, J.C. Hernadez-Garrido, J.M. Gonzalez-Leal, M.A. Cauqui, M.P. Yeste, Highly stable ceria-zirconia-yttria supported Ni catalysts for syngas production by CO_2 reforming of methane, Appl. Surf. Sci. 426 (2017) 864-873.

9.   R. Horn, R. Schlogl, Methane activation by heterogeneous catalysis, Catal. Lett. 145 (2015) 23-39.

10.   B.R. De Vasconcelos, L. Zhao, P. Sharrock, A. Nzihou, D.P. Minh, Catalytic transformation of carbon dioxide and methane into syngas over ruthenium and platinum supported hydroxyapatites, Appl. Surf. Sci. 390 (2016) 141-156.

11.   W. Li, Z. Zhao, Y. Jiao, Dry reforming of methane towards CO-rich hydrogen production over robust supported Ni catalyst on hierarchically structured monoclinic zirconia nanosheets, Int. J. Hydrogen Energ. 41 (2016) 17907-17921.

12.   X. Xiang, H. Zhao, J. Yang, J. Zhao, L. Yan, H. Song, L., Nickel based mesoporous silica-ceria-zirconia composite for carbon dioxide reforming of methane, Appl. Catal. A. 520 (2016) 140-150.

13.   S. Ali, M.J. Al-Marri, A.G. Abdelmoneim, A. Kumar, M.M. Khader, Catalytic evaluation of nickel nanoparticles in methane steam reforming, Int. J. Hydrogen Energ. 41 (2016) 22876-22885.

14.   O.A. Bereketidou, M.A. Goula, Biogas reforming for syngas production over nickel supported on ceria-alumina catalysts, Catal. Today 195 (2012) 93-100.

15.   A.A. Lemonidou, M.A. Goula, I.A. Vasalos, Carbon dioxide reforming of methane over 5 wt.% nickel calcium aluminate catalysts - Effect of preparation method, Catal. Today 46 (1998) 175-183.

16. M.A. Goula, A.A. Lemonidou, A.M. Efstathiou, Characterization of carbonaceous species formed during reforming of CH_4 with CO_2 over Ni/CaO-Al_2O_3 catalysts studied by various transient techniques, J. Catal. 161 (1996) 626-640.

17. M.A. Goula, A.A. Lemonidou, W. Grunert, M. Baerns, Methane partial oxidation to synthesis gas using nickel on calcium aluminate catalysts, Catal. Today 32 (1996) 149-156.

18. C. Italiano, R. Balzarotti, A. Vita, S. Latorrata, C. Fabiano, L. Pino, C. Cristiani, Preparation of structured catalysts with Ni and Ni–Rh/CeO_2 catalytic layers for syngas production by biogas reforming processes, Catal. Today 273 (2016) 3-11.

19. C.A. Schwengber, F.A. da Silva, R.A. Schaffner, N.R.C. Fernandes-Machado, R.J. Ferracin, V.R. Bach, H.J. Alves, Methane dry reforming using Ni/Al_2O_3 catalysts: Evaluation of the effects of temperature, space velocity and reaction time, J. Environ. Chem. Eng. 4 (2016) 3688-3695.

20. N.A.K. Aramouni, J. Zeaiter, W. Kwapinski, M.N. Ahmad, Thermodynamic analysis of methane dry reforming: Effect of the catalyst particle size on carbon formation, Energ. Convers. Manage. 150 (2017) 614-622.

21. N. Habibi, Y. Wang, H. Arandiyan, M. Rezaei, Effect of substitution by Ni in $MgAl_2O_4$ spinel for biogas dry reforming, Int. J. Hydrogen Energ. 42 (2017) 24159-24168.

22. X. Chen, J. Jiang, K. Li, S. Tian, F. Yan, Energy-efficient biogas reforming process to produce syngas: The enhanced methane conversion by O_2, Appl. Energy 185 (2017) 687-697.

23. M. Luneau, E. Gianotti, F.C. Meunier, C. Mirodatos, E. Puzenat, Y. Schuurman, N. Guilhaume, Deactivation mechanism of Ni supported on Mg-Al spinel during autothermal reforming of model biogas, Appl. Catal. B 203 (2017) 289-299.

24. J. Juan-Juan, M.C. Roman-Martinez, M.J. Illan-Gomez, Nickel catalyst activation in the carbon dioxide reforming of methane: Effect of pretreatments, Appl. Catal. A 355 (2009) 27-32.

25. M.A. Goula, N.D. Charisiou, K.N. Papageridis, A. Delimitis, E. Pachatouridou, E.F. Iliopoulou, Nickel on alumina catalysts for the production of hydrogen rich mixtures via the biogas dry reforming reaction: Influence of the synthesis method, Int. J. Hydrogen Energ. 40 (2015) 9183-9200.

26. M.A. Goula, N.D. Charisiou, K.N. Papageridis, G. Siakavelas, Hydrogen via the glycerol steam reforming reaction: Influence of the synthesis method for Ni/Al_2O_3 catalysts, Chin. J. Catal. 37 (2016) 1949-1965.

27. J.A. Montoya, E. Romero-Pascual, C. Gimon, P. Del Angel, A. Monzon, Methane reforming with CO_2 over Ni/ZrO_2–CeO_2 catalysts prepared by sol–gel, Catal. Today 63 (2000) 71-85.

28. Y. Zhan, J. Han, Z. Bao, B. Cao, Y. Li, J. Street, F. Yu, Recent advances in dry reforming of methane over Ni-based catalysts, Mol. Catal. 436 (2017) 248-258.

29. Y. Kathiraser, Z. Wang, M.L. Ang, L. Mo, Z. Li, U. Oemar, S. Kawi, Highly active and coke resistant Ni/SiO$_2$ catalysts for oxidative reforming of model biogas: Effect of low ceria loading, J. CO$_2$ Util. 19 (2017) 284-295.

30. S.A. Theofanidis, V.V. Galvita, H. Poelman, G.B. Marin, Enhanced carbon-resistant dry reforming Fe-Ni catalyst: Role of Fe, ACS Catal. 5 (2015) 3028-3039.

31. X. Zhao, H. Li, J. Zhang, L. Shi, D. Zhang, Design and synthesis of NiCe@m-SiO$_2$ yolk-shell framework catalysts with improved coke- and sintering-resistance in dry reforming of methane, Int. J. Hydrogen Energ. 41 (2016) 2447-2456.

32. U. Oemar, K. Hidajat, S. Kawi, Pd–Ni catalyst over spherical nanostructured Y$_2$O$_3$ support for oxy-CO2 reforming of methane: Role of surface oxygen mobility, Int. J. Hydrogen Energ. 40 (2015) 12227-12238.

33. M. Yu, Y.A. Zhu, Y Lu, G. Tong, K. Zhu, X. Zhou, The promoting role of Ag in Ni-CeO$_2$ catalyzed CH$_4$-CO$_2$ dry reforming reaction, Appl. Catal. B 165 (2015) 43-56.

34. X.E. Verykios, Catalytic dry reforming of natural gas for the production of chemicals and hydrogen, Int. J. Hydrogen Energ. 28 (2003) 1045-1063.

35. J.D.A. Bellido, J.E. De Souza, J.C. M'Peko, E.M. Assaf, Effect of adding CaO to ZrO$_2$ support on nickel catalyst activity in dry reforming of methane, Appl. Catal. A 358 (2009) 215-223.

36. J.D.A. Bellido, E.M. Assaf, Effect of the Y$_2$O$_3$–ZrO$_2$ support composition on nickel catalyst evaluated in dry reforming of methane, Appl. Catal. A 352 (2009) 179-187.

37. M. Rezaei, S.M. Alavi, S. Sahebdelfar, Z.-F. Yan, Effects of K$_2$O promoter on the activity and stability of nickel catalysts supported on mesoporous nanocrystalline zirconia in CH$_4$ reforming with CO$_2$, Energ. Fuel. 22 (2008) 2195-2202.

38. E.N. Alvara, M. Rezaei, Mesoporous nano-crystalline MgAl$_2$O$_4$ spinel and its applications as support for Ni catalyst in dry reforming, Scripta Mater. 61 (2009) 212-215.

39. Z. Alipour, M. Rezaei, F. Meshkani, Effect of Ni loadings on the activity and coke formation of MgO-modified Ni/Al$_2$O$_3$ nano-catalyst in dry reforming of methane, J. Energy Chem. 23 (2014) 633-638.

40. F. Mirzaei, M. Rezaei, F. Meshkani, Z. Fattah, Carbon dioxide reforming of methane for syngas production over Co–MgO mixed oxide nanocatalysts, J. Ind. Eng. Chem. 21 (2015) 662-667.

41. M.A. Goula, Ch. Kordulis, A. Lycourghiotis, Influence of impregnation parameters on the axial Mo/γ-alumina profiles studied using a novel simple technique, J. Catal. 133 (1992) 486-497.

42. Y. Asencios, K. Elias, E.M. Assaf, Oxidative-reforming of model biogas over NiO/Al$_2$O$_3$ catalysts: The influence of the variation of support synthesis conditions, Appl. Surf. Sci. 317 (2014) 350–359.

43. N.D. Charisiou, G. Siakavelas, K.N. Papageridis, A. Baklavaridis, L. Tzounis, D.G. Avraam, M.A. Goula, Syngas production via the biogas dry reforming reaction over nickel supported on modified with CeO_2 and/or La_2O_3 alumina catalysts, J. Nat. Gas Sci. Eng. 31 (2016) 164-183.

44. N.D. Charisiou, G. Siakavelas, K.N. Papageridis, A. Baklavaridis, L. Tzounis, K. Polychronopoulou, M.A. Goula, Hydrogen production via the glycerol steam reforming reaction over nickel supported on alumina and lanthana-alumina catalysts, Int. J. Hydrogen Energ. 42 (2017) 13039-13060.

45. R. Martínez, R. Romero, C. Guimon, R. Bilbao, CO_2 reforming of methane over coprecipitated Ni-Al catalysts modified with lanthanum, Appl. Catal. A 274 (2004) 139-149.

46. Z.W. Liu, H.S. Roh, K.W. Jun, Carbon dioxide reforming of methane over Ni/La_2O_3 /Al_2O_3, J. Ind. Eng. Chem. 9 (2003) 267-274.

47. A. Slagtern, Y. Schuurman, C. Leclercq, X. Verykios, C. Mirodatos, Specific features concerning the mechanism of methane reforming by carbon dioxide over Ni/La_2O_3 catalyst, J. Catal. 256 (1997) 124-129.

48. R. Benrabaa, A. Barama, H. Boukhlouf, J. Guerrero-Caballero, A. Rubbens, E. Bordes-Richard, A. Lofberg, R.-N. Vannier, Physico-chemical properties and syngas production via dry reforming of methane over $NiAl_2O_4$ catalyst, Int. J. Hydrogen Energ 42 (2017) 12989-12996.

49. Z. Shang, S. Li, L. Li, G. Liu, X. Liang, Highly active and stable alumina supported nickel nanoparticle catalysts for dry reforming of methane, Appl. Catal. B-Environ. 201 (2017) 302-309.

50. A.S.B. Neto, A.C. Oliveira, J.M. Filho, N. Amadeo, M.L. Dieuzeide, F.F. de Sousa, A.C. Oliveira, Characterizations of nanostructured nickel aluminates as catalysts for conversion of glycerol: Influence of the preparation methods, Adv. Powder Technol. 28 (2017) 131-138.

51. M. Thommes, K. Kaneko, A.V. Neimark, J.P. Olivier, R.F. Rodriguez, J. Rouquerol, K.S.W. Sing, Physisorption of gases, with special reference to the evaluation of surface area and pore size distribution. Eds. Burrows, Hugh / Weir, Ron / Stohner, Jürgen; 2015.

52. J.H. Lehman, M. Terrones, E. Mansfield, K.E. Hurst, V. Meunier, Evaluating the characteristics of multiwall carbon nanotubes, Carbon 49 (2011) 2581-2602.

53. M. Velasquez, C. Batiot-Dupeyrat, L. Gallego, A. Santamaria, Chemical and morphological characterization of multi-walled-carbon nanotubes synthesized by carbon deposition from an ethanol–glycerol blend, Diam. Relat. Mater. 50 (2014) 38-48.

54. C.J. Liu, J. Ye, J Jiang, Y. Pan, Progresses in the preparation of coke resistant Ni-based catalyst for steam and CO_2 reforming of methane. ChemCatChem 3 (2011) 529-541.

55. H.R. Gurav, S. Dama, V. Samuel, S. Chilukuri, Influence of preparation method on activity and stability of Ni catalysts supported on Gd doped ceria in dry reforming of methane, J. CO_2 Util. 20 (2017) 357-367.

56. J. Li, X. Tang, H. Yi, Q. Yu, F. Gao, R. Zhang, C. Li, C. Chu, Effects of copper-precursors on the catalytic activity of Cu/graphene catalysts for the selective catalytic oxidation of ammonia, Appl. Surf. Sci. 412 (2017) 37-44.

57. M. Pudukudy, Z. Yaakob, Z.S. Akmal, Direct decomposition of methane over SBA-15 supported Ni, Co and Fe based bimetallic catalysts, Appl. Surf. Sci. 330 (2015) 418-430.

58. M. Pudukudy, Z. Yaakob, Z.S. Akmal, Direct decomposition of methane over Pd promoted Ni/SBA-15 catalysts, Appl. Surf. Sci. 353 (2015) 127-136.

59. R. Baddour-Hadjean, J.P. Pereira-Ramos, Raman Microspectrometry Applied to the Study of Electrode Materials for Lithium Batteries, Chem. Rev. 110 (2010) 1278-1319.

60. R. Saito, A. Gruneis, G.S. Ge, V.W. Brar, G. Dresselhaus, M.S. Dresselhaus, A. Jorio, L.G. Cancado, C. Fantini, M.A. Pimenta, Double resonance Raman spectroscopy of single-wall carbon nanotubes, New J. Phys. 5 (2003) 157.1-157.15.

61. M. Garcia-Dieguez, I.S. Pieta, M.C. Herrera, M.A. Larrubia, L.J. Alemany, Improved Pt-Ni nanocatalysts for dry reforming of methane, Appl. Catal. A 377 (2010) 191-199.

62. Y. Liu, C. Pan, J. Wang, Raman spectra of carbon nanotubes and nanofibers prepared by ethanol flames, J. Mater. Sci. 39 (2004) 1091-1094.

63. M. Pudukudy, Z. Yaakob, S. Takriff, Methane decomposition over Pd promoted $Ni/MgAl_2O_4$ catalysts for the production of CO_x free hydrogen and multiwalled carbon nanotubes, Appl. Surf. Sci. 356 (2015) 1320-1326.

64. A.E. Awadallah, A.A. Aboul-Enein, D.S. El-Desouki, A.K. Aboul-Gheit, Catalytic thermal decomposition of methane to CO_x-free hydrogen and carbon nanotubes over MgO supported bimetallic group VIII catalysts, Appl. Surf. Sci. 296 (2014) 100-107.

65. K. Sutthiumporn, S. Kawi, Promotional effect of alkaline earth over $Ni–La_2O_3$ catalyst for CO_2 reforming of CH_4: Role of surface oxygen species on H_2 production and carbon suppression, Int. J. Hydrogen Energ. 36 (2011) 14435-14446.

66. E.F. Antunes, A.O. Lobo, E.J. Corat, V.J. Trava-Airoldi, A.A. Martin, C. Verissiomo, Comparative study of first- and second-order Raman spectra of MWCNT at visible and infrared laser excitation, Carbon 44 (2006) 2202-2211.

67. K.T.Ng, D.M. Hercules, Studies of nickel-tungsten-alumina catalysts by X-ray photoelectron spectroscopy, J. Phys. Chem. 80 (1976) 2094-2102

68. D.A.J.M. Ligthart, J.A.Z. Pieterse, E. J.M. Hensen, The role of promoters for Ni catalysts in low temperature (membrane) steam methane reforming, Appl. Catal. A 405 (2011) 108-119.

69. M.A. Goula, N.D. Charisiou, G. Siakavelas, L. Tzounis, I. Tsiaoussis, P. Panagiotopoulou, G. Goula, I.V. Yentekakis, Syngas production via the biogas dry reforming reaction over Ni supported on zirconia modified with CeO_2 or La_2O_3 catalysts, Int. J. Hydrogen Energ. 42 (2017) 13724-13740.

70. B. Abdullah, N.A.A. Ghani, D.V.N. Vo, Recent advances in dry reforming of methane over Ni-based catalysts, J. Clean. Prod. 162 (2017) 170-185.

71. H. Silvester. A. de Sousa, A.N. da Silva, A.J.R. Castro, A. Campos, J.M. Filho, A.C. Oliveira, Mesoporous catalysts for dry reforming of methane: Correlation between structure and deactivation behavior of Ni-containing catalysts, Int. J. Hydrogen Energ. 37 (2012) 12281-12291

72. A. Mezzi, K. Kaciulis, Surface investigation of carbon films: from diamond to graphite, Surf. Interface Anal. 42 (2010) 1082-1084.

73. P.O. Vargas, N.A.F. González, R.M. Navarro, J.L.G. Fierro, C.H. Campos, P. Reyes, Improved stability of Ni/Al_2O_3 catalysts by effect of promoters (La_2O_3, CeO_2) for ethanol steam-reforming reaction, Catal. Today 259 (2015) 27–38.

74. M.K. Nikoo, N.A.S. Amin, Thermodynamic analysis of carbon dioxide reforming of methane in view of solid carbon formation, Fuel Process. Technol. 92 (2011) 678-691.

75. A. Gao, R. Lu, G. Veser, Stabilizing metal nanoparticles for heterogeneous catalysts, Phys. Chem. Chem. Phys. 12 (2010) 13499-13510.

76. F. Meshkani, M. Rezaei, Ni catalysts supported on nanocrystalline magnesium oxide for syngas production by CO_2 reforming of CH_4, J. Nat. Gas Chem. 20 (2011) 198-203.

77. F. Meshkani, M. Rezaei, Nickel catalyst supported on magnesium oxide with high surface area and plate-like shape: a highly stable and active catalyst in methane reforming with carbon dioxide, Catal. Commun. 12 (2011) 1046-1050.

78. K. Jabbour, P. Massiani, A. Davidson, S. Casale, N. El Hassan, Ordered mesoporous "one-pot" synthesized Ni-Mg(Ca)-Al_2O_3 as effective and remarkably stable catalysts for combined steam and dry reforming of methane (CSDRM), Appl. Catal. B 201 (2017) 527-542.

79. N. Aramouni, J. Zeaiter, W. Kwapinski, M.N. Ahmad, Thermodynamic analysis of methane dry reforming: Effect of the catalyst particle size on carbon formation, Energ Convers and Manage 150 (2017) 614–622

80. A.S. Al-Fatesh, Y. Arafat, H. Atia, A.A. Ibrahim, Q.L.M. Ha, M. Schneider, M. M-Pohl, A.H. Fakeeh, CO_2-reforming of methane to produce syngas over Co-Ni/SBA-15 catalyst: Effect of support modifiers (Mg, La and Sc) on catalytic stability, J. CO_2 Util. 21 (2017) 395–404

81. S. Bang, E. Hong, S.W. Baek, C-H Shin, Effect of acidity on Ni catalysts supported on P-modified Al_2O_3 for dry reforming of methane, Catal. Today, in press.

82. Y. Wang, L. Yao, S. Wang, D. Mao, C. Hu, Low-temperature catalytic CO_2 dry reforming of methane on Ni-based catalysts: A review, Fuel Process. Technol. 169 (2018) 199–206.

83. M. Akri, S. Pronier, T. Chafik, O. Achak, P. Granger, P. Simon, M. Trentesaux, C. Batiot-Dupeyrat, Development of nickel supported La and Ce-natural illite clay for autothermal dry reforming of methane: Toward a better resistance to deactivation, Appl. Catal. B 205 (2017) 519–531.

84. X. Li, D. Li, H. Tian, L. Zeng, Z.J. Zhao, J. Gong, Dry reforming of methane over Ni/La_2O_3 nanorod catalysts with stabilized Ni nanoparticles, Appl. Catal. B 202 (2017) 683-694.

85. U. Oemar, Y. Kathiraser, L. Mo, X.K. Ho, S. Kawi, CO_2 reforming of methane over highly active La-promoted Ni supported on SBA-15 catalysts: mechanism and kinetic modeling, Catal. Sci. Technol. 6 (2016) 1173-1186.

86. Z. Zhang, X.E. Verykios, S.M. MacDonald, S. Affrossman, Comparative study of carbon dioxide reforming of methane to synthesis gas over Ni/La_2O_3 and conventional nickel-based catalysts, J. Phys. Chem. 100 (1996) 744-754.

Fig. 1: (a,b) TEM images, (c) Scheme of the catalyst structure, (d) Particle size distribution histogram, (e,f) STEM-HAADF images with Z-contrast (heavy atoms have high brightness), (g) EDS spectra of areas marked in (f) for the Ni/LaAl catalyst; (h) STEM-HAADF images with Z-contrast, (i) EDS spectra of areas marked in (h), (j) Scheme of the catalyst structure, (k) Particle size distribution histogram for the Ni/Al catalyst.

Fig 2. Pore size distribution and N_2 adsorption–desorption isotherms (inset) of the reduced and spent catalysts at 600, 700 and 800°C.

Fig. 3: DTG graphs of the spent Ni/Al and Ni/LaAl catalysts.

Fig. 4: Raman spectra of spent Ni/Al and Ni/LaAl catalysts.

Fig. 5: TEM images of spent Ni/Al (a,b) and Ni/LaAl (c,d) catalysts.

Fig. 6: HR-TEM images of spent Ni/Al (a) and Ni/LaAl (b) catalyst.

Fig. 7: The Ni2p region of the XPS spectra for the Ni/Al (a) and Ni/LaAl (b) spent catalysts.

Fig. 8: The C 1s region of the XPS spectra for the Ni/Al (a) and Ni/LaAl (b) spent catalysts.

Fig. 9: CH_4 and CO_2 conversion (%) for the Ni/Al and Ni/LaAl catalysts for stability tests conducted at different temperatures.

Fig. 10: H_2 and CO yield (%) for the Ni/Al and Ni/LaAl catalysts for stability tests conducted at different temperatures.

Fig. 11: H_2/CO molar ratio for the Ni/Al and Ni/LaAl catalysts for stability tests conducted at different temperatures.
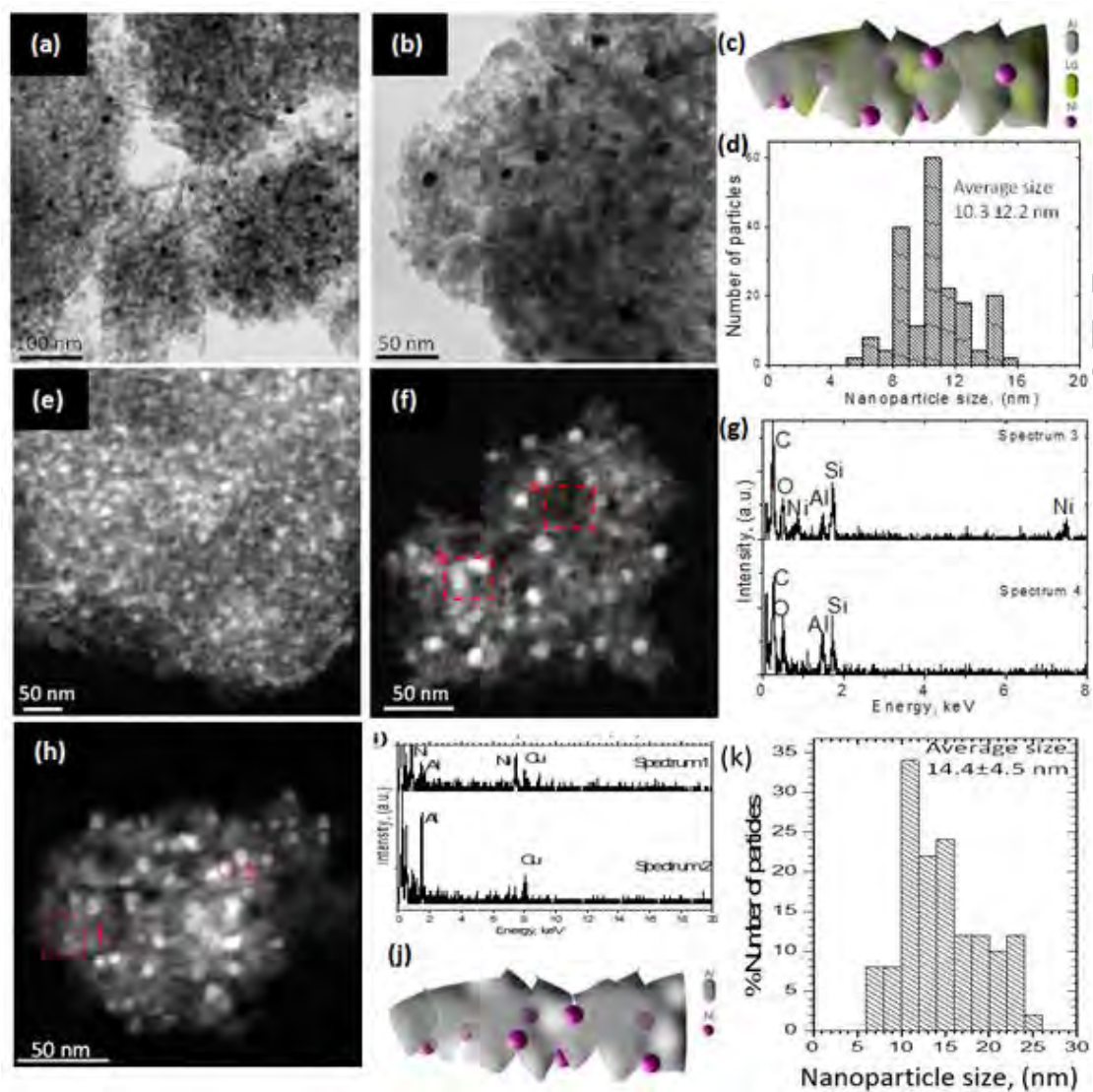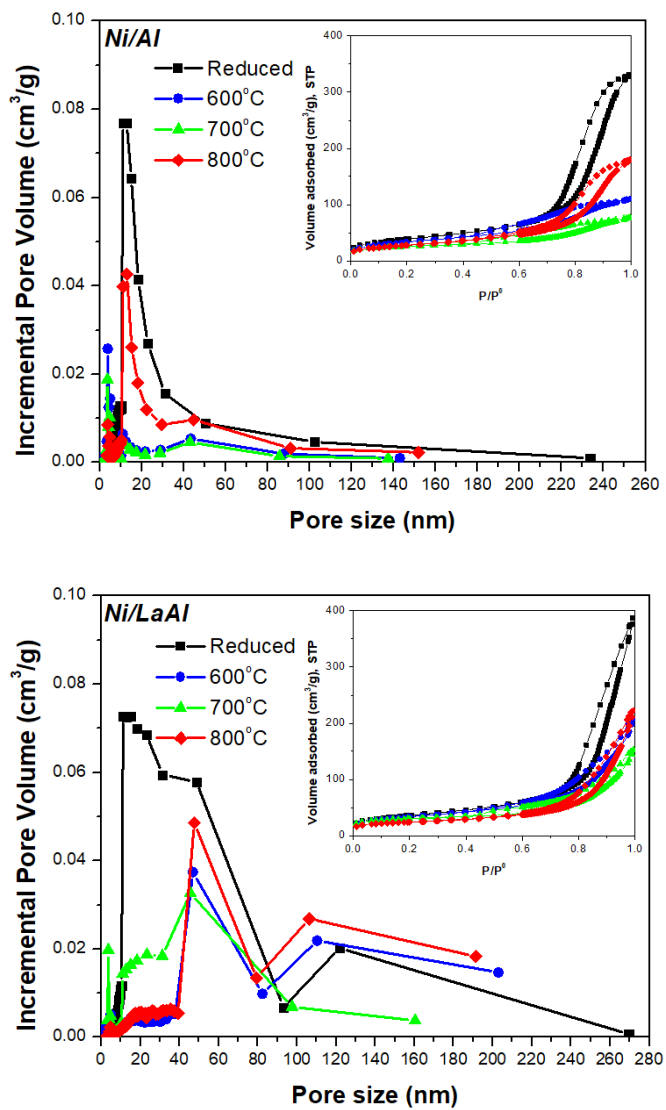
Fig. 1

Fig. 2
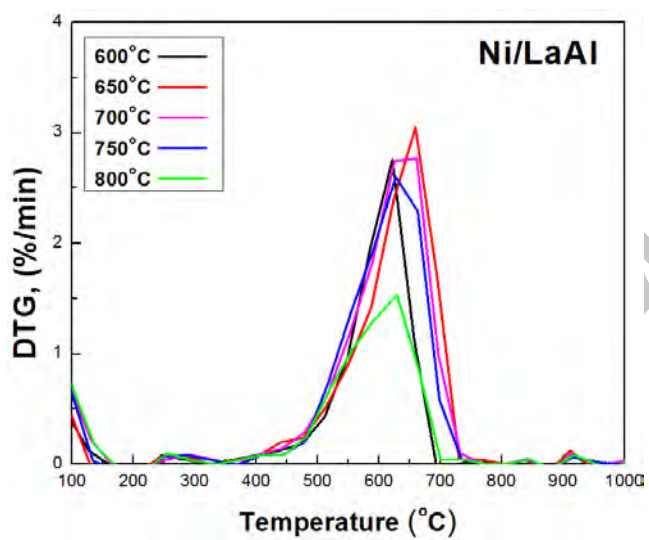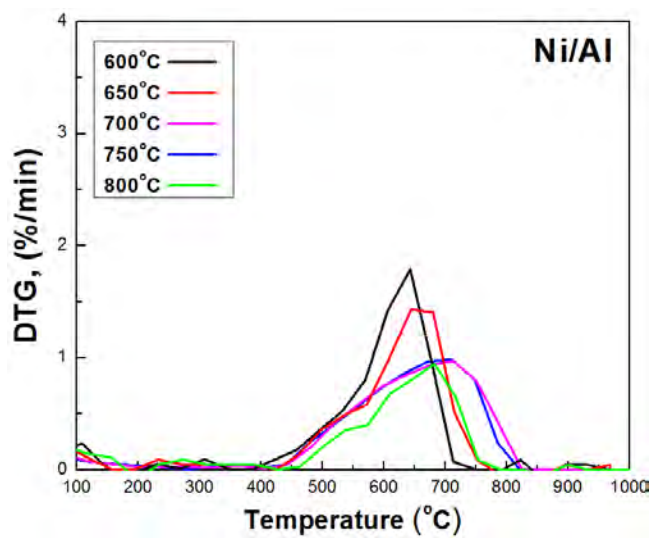
Fig. 3
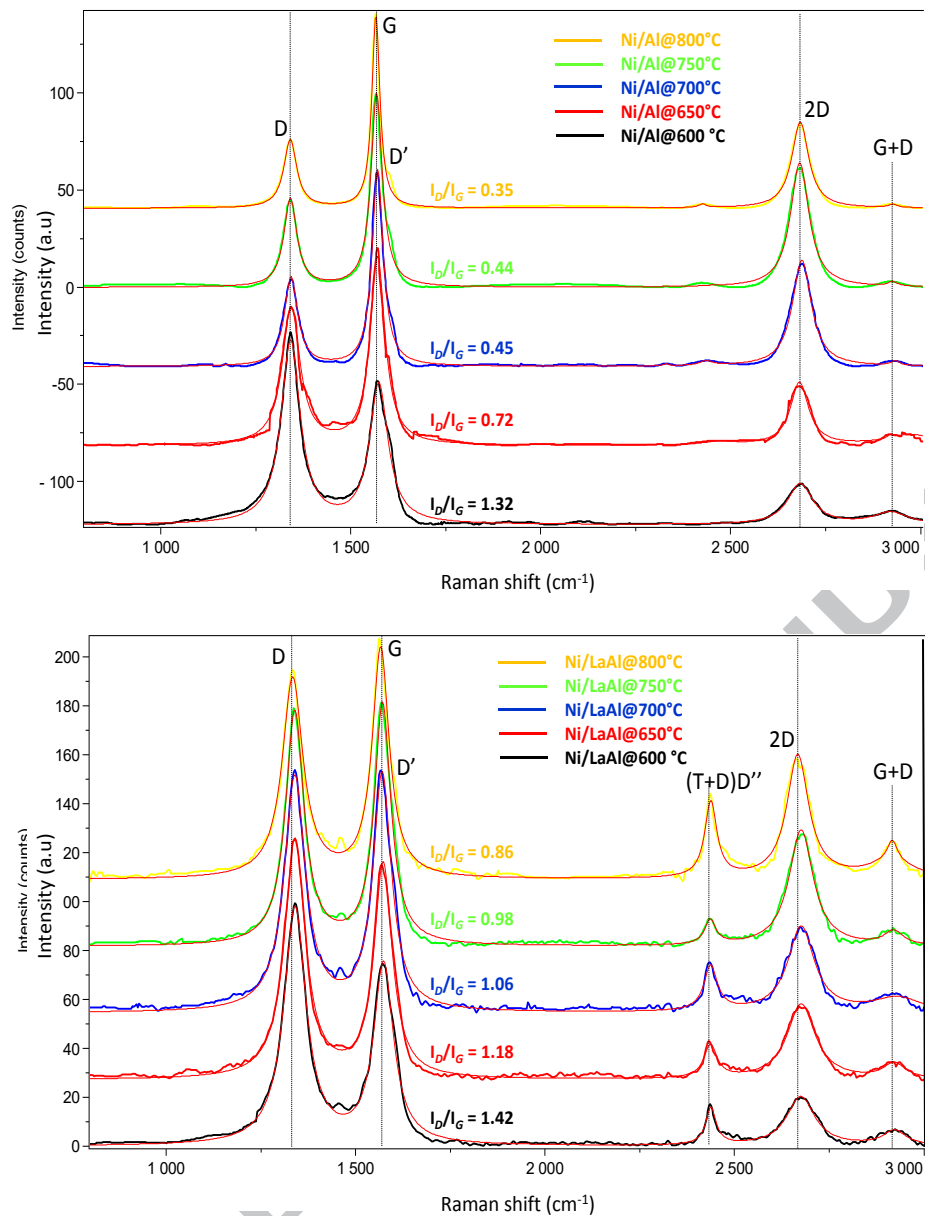
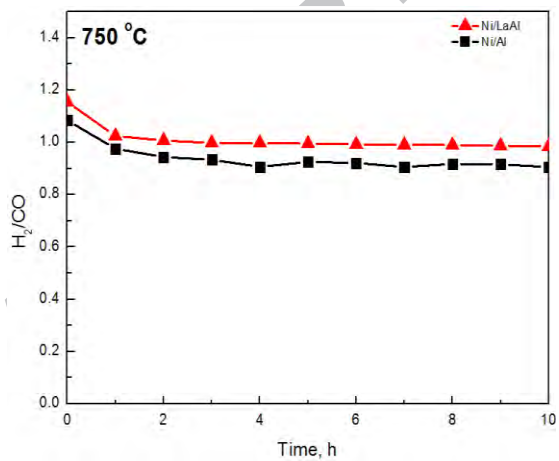**Fig. 4**
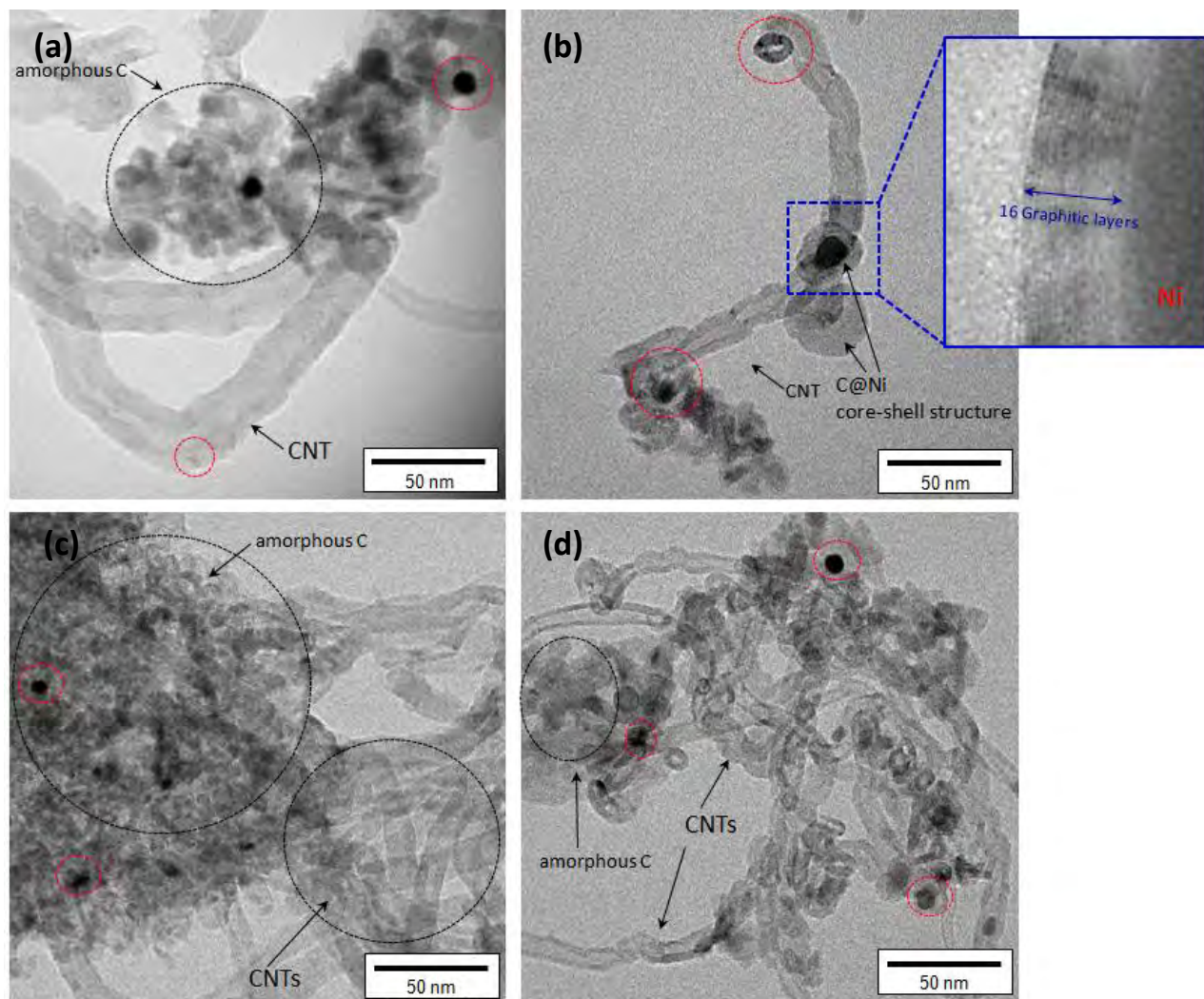
Fig. 5
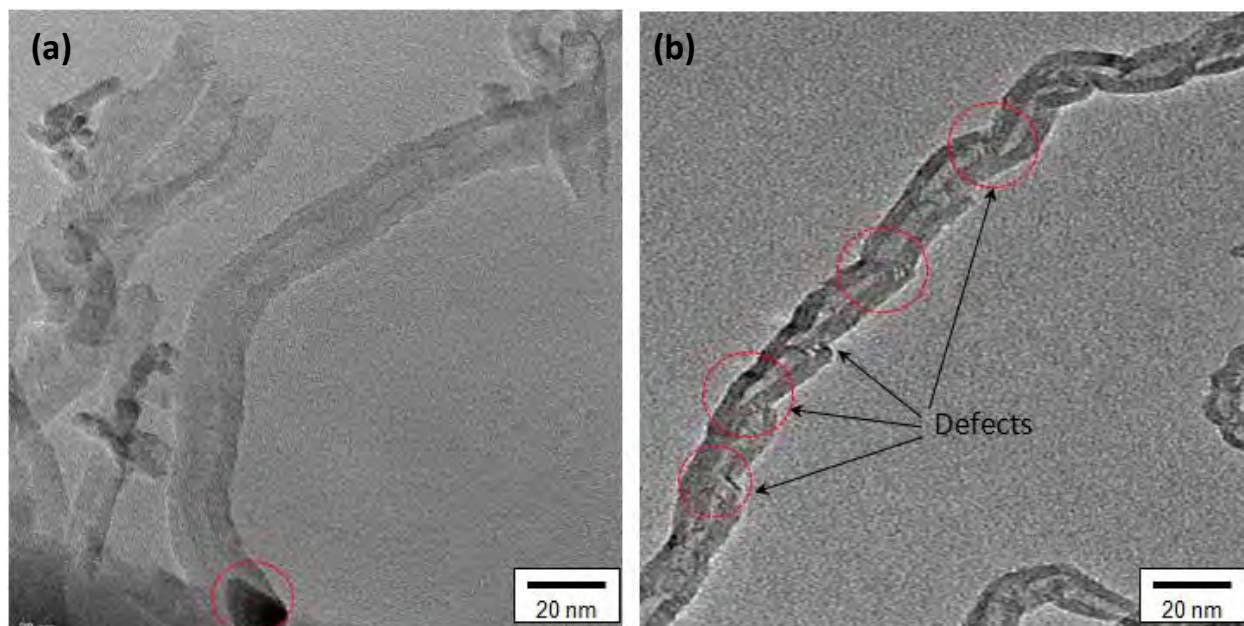
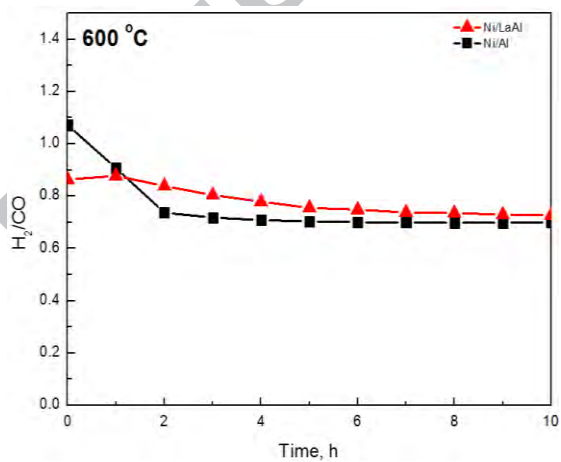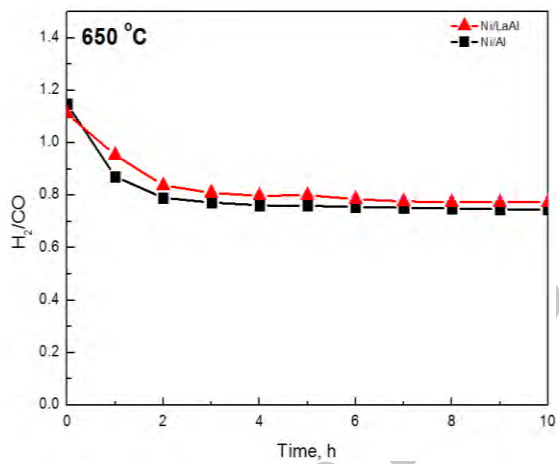**Fig. 6**
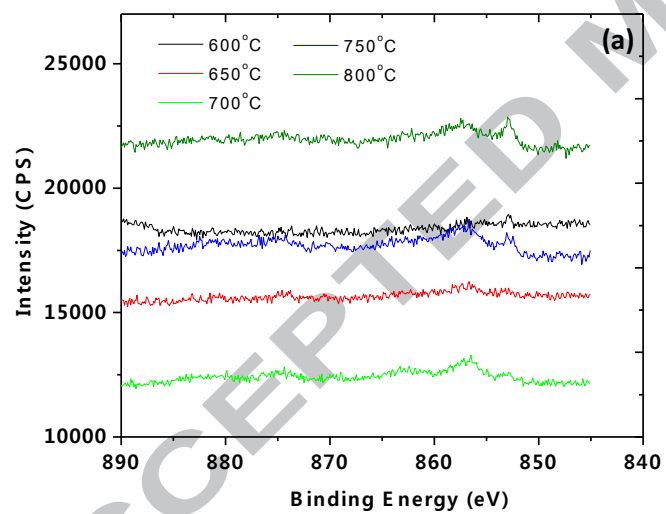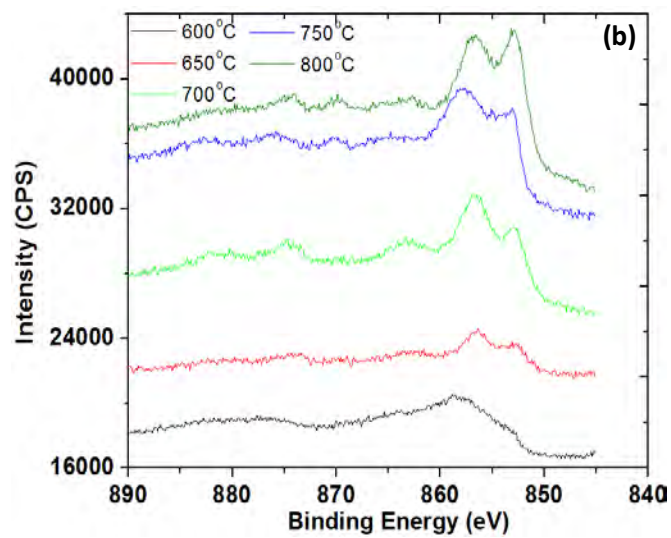
Fig. 7
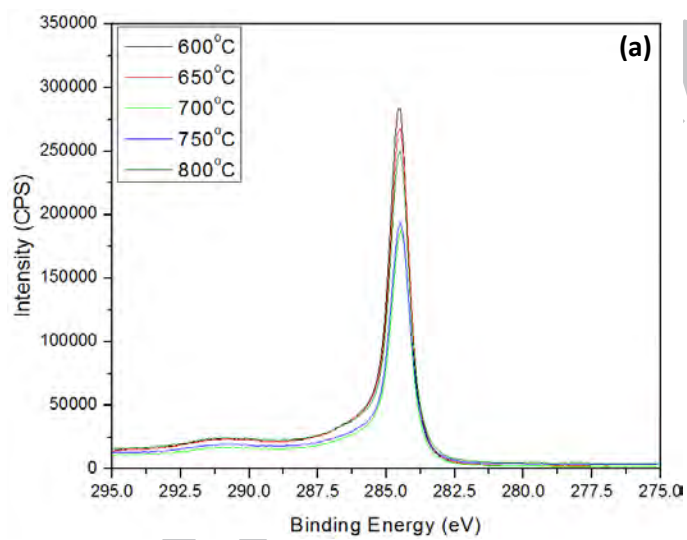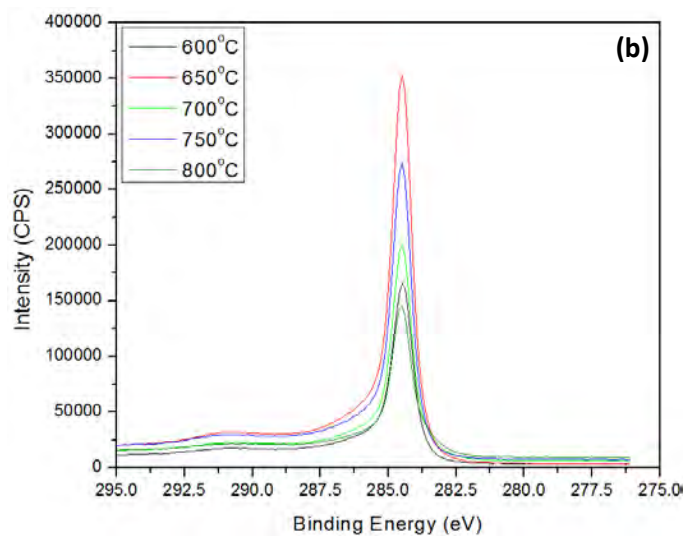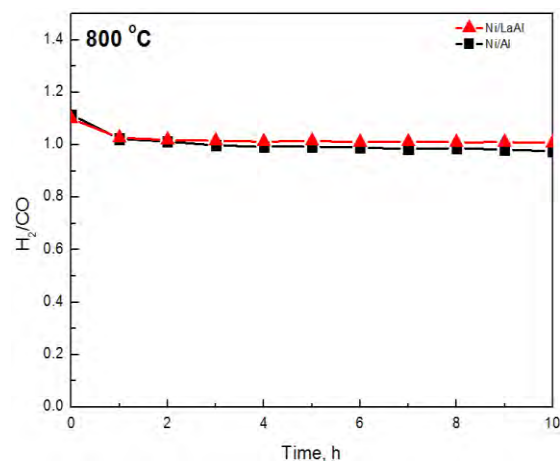
Fig. 8
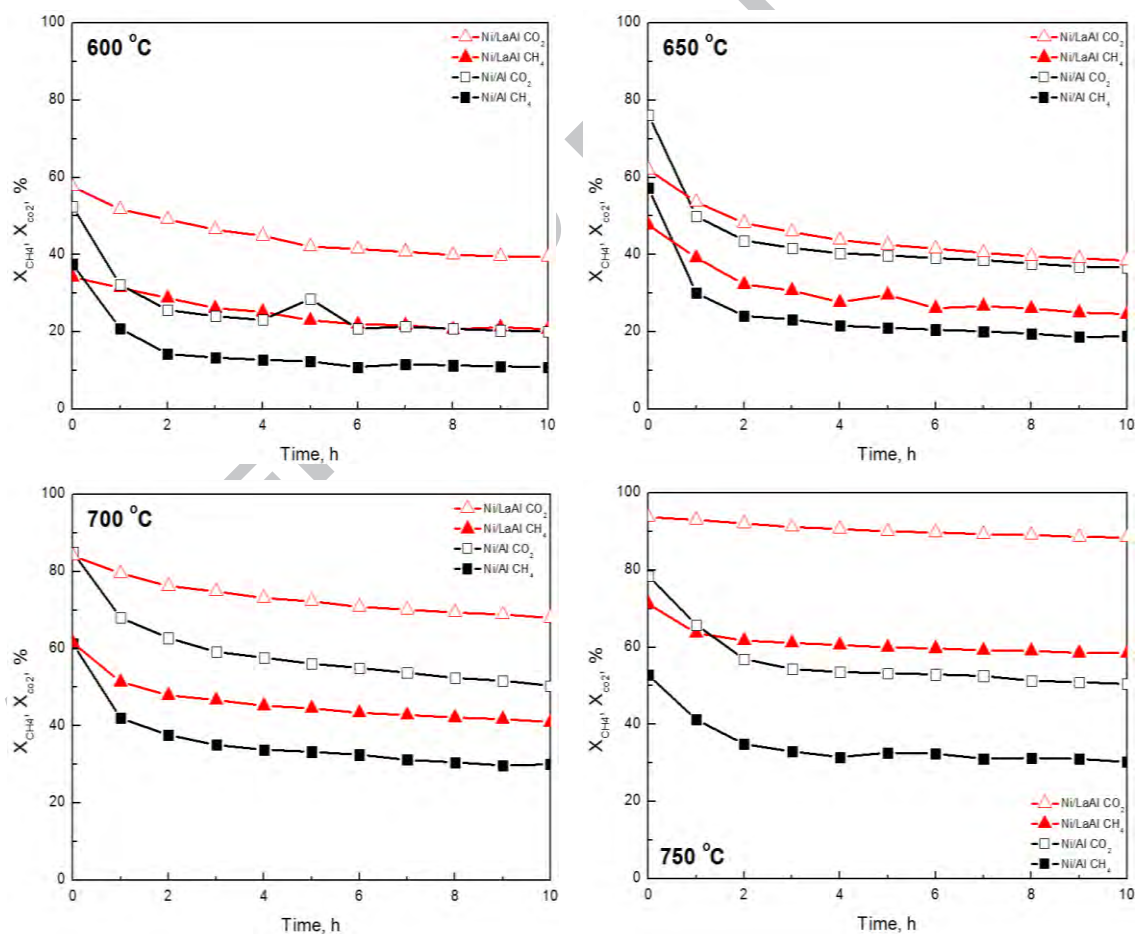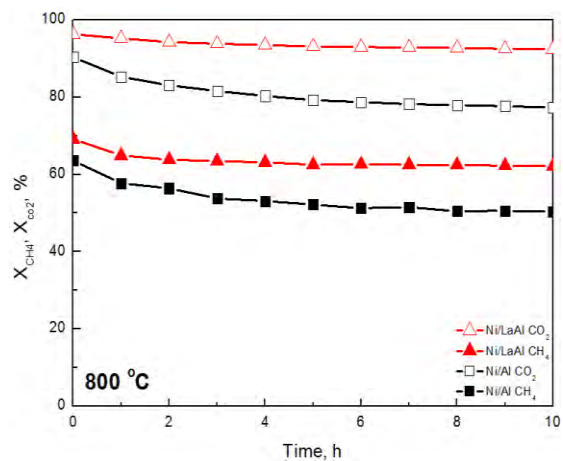
Fig. 9
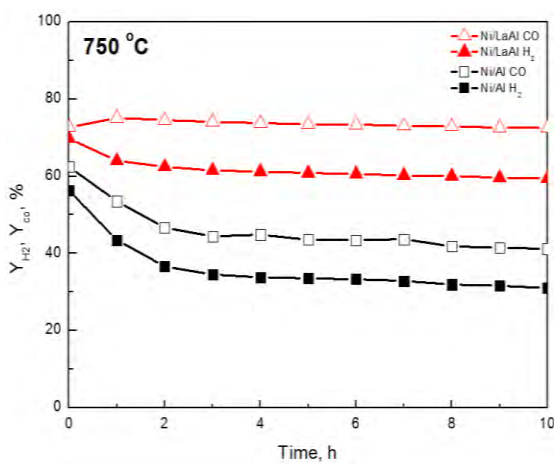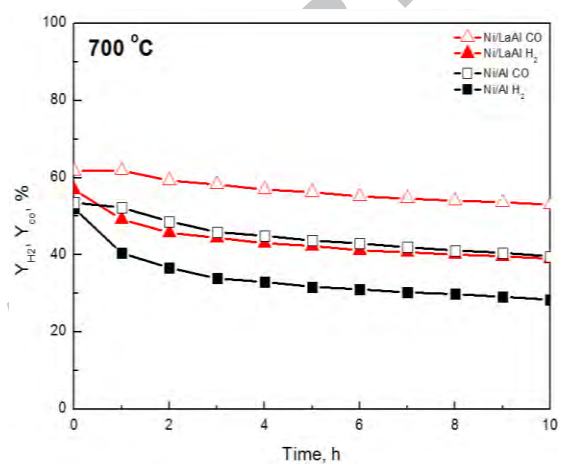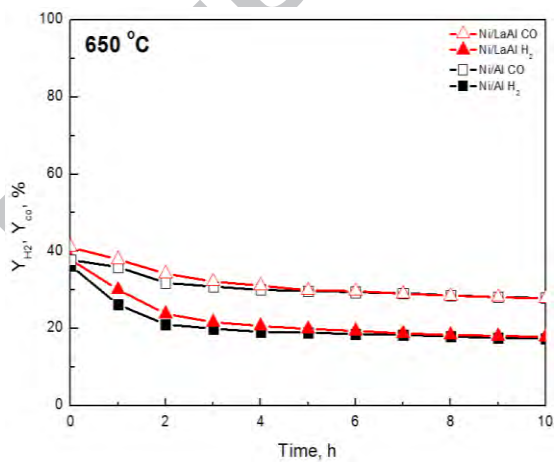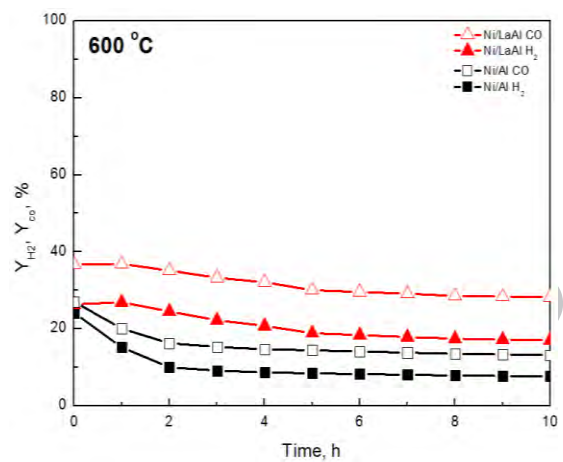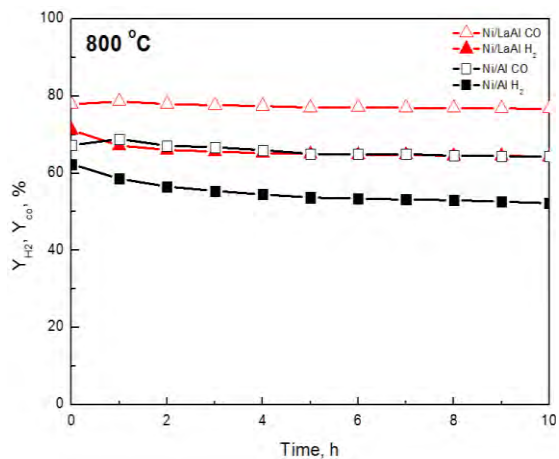
Fig. 10
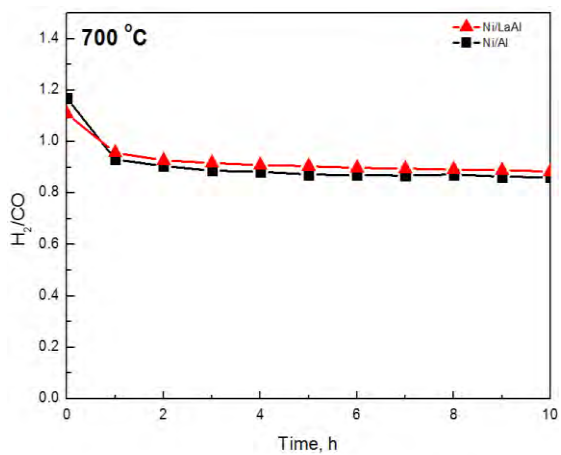
Fig. 11

Table 1: Specific surface area (SSA), pore volume, Average pore width and Ni^0 mean crystallite size (as determined by TEM experiments) for the reduced and spent catalysts at 600, 700 and 800 ^{o}C

Catalyst	SSA (m^2 g^{-1})	Pore volume (cm^3 /g)	Av. pore width (nm)	Ni^0 mean crystallite size (nm)
Ni/Al-r	136	0.32	20.1	14.4±4.5
Ni/Al-600	118	0.08	15.7	17.3±4.3
Ni/Al-700	83	0.06	15.5	*n/a*
Ni/Al-800	98	0.18	15.8	15.2±6.1
Ni/LaAl-r	126	0.43	21.1	10.3±2.2
Ni/LaAl-600	117	0.22	15.8	12.0±5.6
Ni/LaAl-700	97	0.16	16.2	*n/a*
Ni/LaAl-800	81	0.26	17.2	10.1±6.1

Note: r= reduced catalyst, n/a= not available

Table 2: XPS peak binding energies and elemental surface concentrations for the Ni/Al catalyst at different reaction temperatures

Catalyst/ Reaction temperature	Peak	Binding energy (eV)	Concentration (at.%)
Ni/Al – 600°C	Al 2p	74.7	1.2
	C 1s	284.5	91.5
	Fe 2p	710.9	0.6
	O 1s	532.5	5.7

	Peak	Binding Energy (eV)	Concentration (at.%)
	Si 2p	103.6	1.0
Ni/Al – 650°C	Al 2p	74.9	3.8
	C 1s	284.5	86.6
	Ni 2p	856.5	0.1
	O 1s	532.1	8.9
	Si 2p	104.2	0.6
Ni/Al – 700°C	Al 2p	74.8	6.3
	C 1s	284.5	80.2
	Ni 2p	856.7	0.3
	O 1s	531.8	12.6
	Si 2p	104.1	0.6
Ni/Al – 750°C	Al 2p	75.0	12.6
	C 1s	284.5	65.6
	Ni 2p	857.1	0.3
	O 1s	532.0	21.5
Ni/Al – 800°C	Al 2p	74.9	11.9
	C 1s	284.5	66.4
	F 1s	685.6	0.2
	Ni 2p	852.9	0.2
	O 1s	532.0	20.9
	Si 2p	103.5	0.4

Table 3: XPS peak binding energies and elemental surface concentrations for the Ni/LaAl catalyst at different reaction temperatures

Catalyst/ Reaction temperature	Peak	Binding Energy (eV)	Concentration (at.%)
Ni/LaAl – 600°C	Al 2p	74.7	11.2
	C 1s	284.5	67.6
	La 3d$_{5/2}$	839.4	0.2
	Ni 2p$_{3/2}$	858.0	0.8
	O 1s	533.5	20.2
Ni/LaAl – 650°C	Al 2p	74.6	4.6
	C 1s	284.5	85.3
	La 3d$_{5/2}$	836.4	0.1
	Ni 2p$_{3/2}$	856.4	0.4
	O 1s	531.6	9.6
Ni/LaAl – 700°C	Al 2p	74.8	15.5
	C 1s	284.5	55.2

	La 3d$_{5/2}$	836.9	0.2
	Ni 2p$_{3/2}$	856.5	1.0
	O 1s	531.8	28.1
Ni/LaAl – 750°C	Al 2p	75.9	13.4
	C 1s	284.5	60.9
	Cl 2p	199.3	0.3
	La 3d$_{5/2}$	838.7	0.2
	Ni 2p$_{3/2}$	856.6	0.7
	O 1s	533.9	24.5
Ni/LaAl – 800°C	Al 2p	74.9	22.9
	C 1s	284.5	35.8
	Cl 2p	198.0	0.3
	La 3d$_{5/2}$	836.9	0.4
	Ni 2p$_{3/2}$	853.4	1.0
	O 1s	531.8	39.6

Graphical abstract
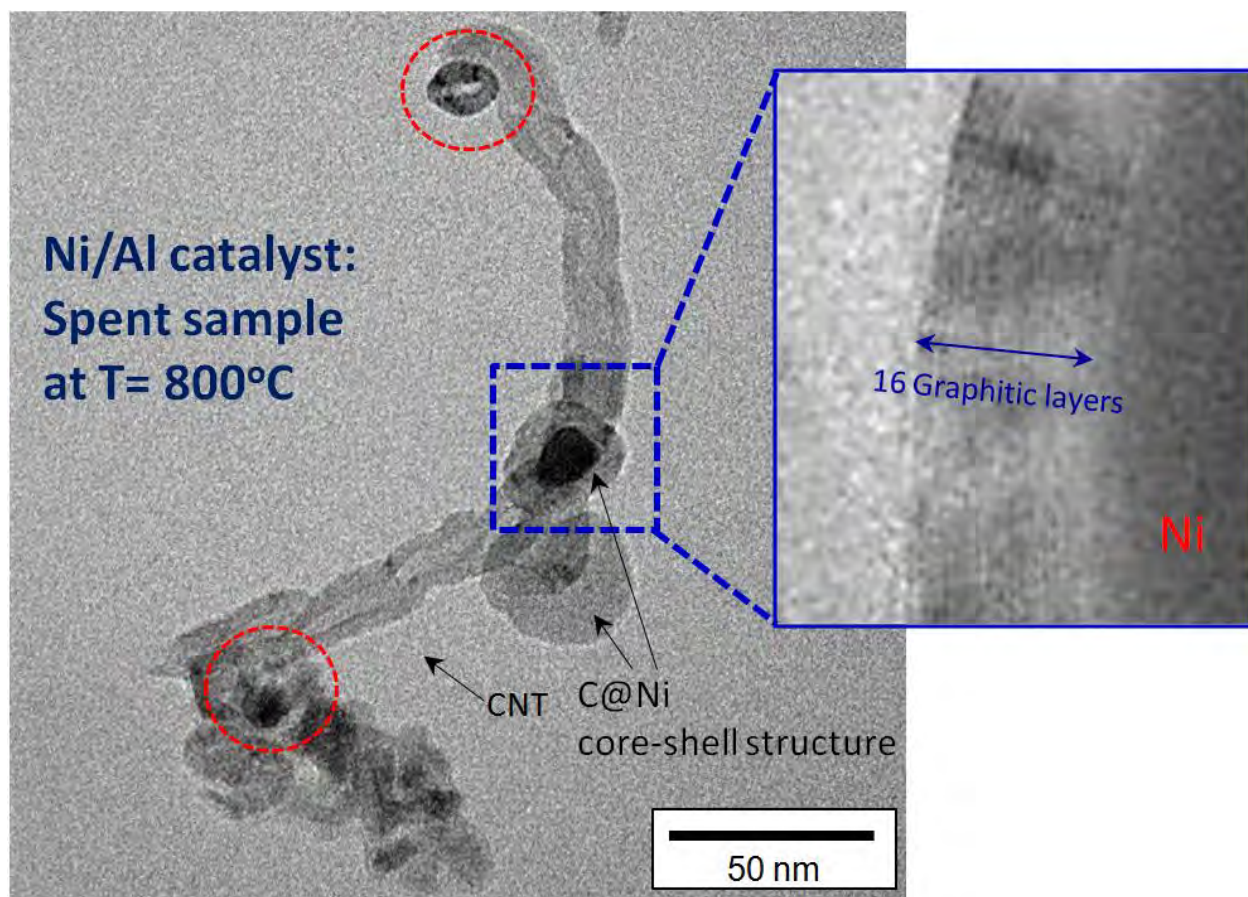
TEM image of the Ni/Al spent catalyst tested at 800°C for the biogas dry reforming reaction. The image clearly shows the formation of carbon nanotubes and core shell structures enclosing the nickel nanoparticles.

Highlights

- Ni/La$_3$O$_3$-Al$_2$O$_3$ catalyst deactivates at a more gradual rate than the Ni/Al$_2$O$_3$
- The presence of La$_2$O$_3$ helps to maintain the Ni^0 active phase during reaction
- Higher Ni and lower C surface concentration for the modified catalyst at all T
- Carbon nanotubes (CNTs) and amorphous carbon were formed over all samples
- Less graphitic and more defective type of deposited carbon for the Ni/LaAl catalyst